Supplementary Information (SI) for Energy & Environmental Science.

Electronic Supplementary Material for

Configurational entropy-tailored NASICON cathode redox chemistry for capacity-dense and ultralong cyclability

Wei Zhang[1,2,7]*, Liang He[3,7], Jiantao Li[4], Ruohan Yu[5], Zhenming Xu[6], Yulun Wu[3], Haotian Qu[2], Qi Zhang[2], Jianwei Li[1], Xian Wu[2], Qingjin Fu[2], Yanqing Lai[3]*, Guangmin Zhou[2]*, Guanjie He[1]* and Ivan P. Parkin[1]

[1] Christopher Ingold Laboratory, Department of Chemistry, University College London, London WC1H 0AJ, UK

[2] Tsinghua Shenzhen International Graduate School, Tsinghua University, Shenzhen 518000, P. R. China

[3] School of Metallurgy and Environment, Central South University, Changsha 410083, P. R. China

[4] Chemical Sciences and Engineering Division, Argonne National Laboratory, Lemont, Illinois 60439, USA

[5] Wuhan University of Technology, The Sanya Science and Education Innovation Park, Sanya 572000, P. R. China

[6] Jiangsu Key Laboratory of Electrochemical Energy Storage Technologies, College of Materials Science and Technology, Nanjing University of Aeronautics and Astronautics, Nanjing 210016, P. R. China

[7] These authors contributed equally.

Methods

Materials synthesis. All samples were synthesized *via* a sol-gel method. All chemicals were directly used without any purification. Specifically, 2.882 g of anhydrous citric acid (≥99.5%, Sigma-Aldrich), 0.878 g of NH_4VO_3 (≥99.0%, Sigma-Aldrich), 0.2 g of $Cr(NO_3)_3·9H_2O$ (≥99.0%, Sigma-Aldrich), 0.123 g of $(CH_3COO)_2Mn·4H_2O$ (≥99.0%, Sigma-Aldrich), 0.204 g of $Fe(NO_3)_3·9H_2O$ (≥98%, Sigma-Aldrich), 0.188 g of $Al(NO_3)_3·9H_2O$ (≥98%, Sigma-Aldrich), 0.107 g of $(CH_3COO)_2Mg·4H_2O$ (≥99%, Sigma-Aldrich), 1.312 g of CH_3COONa (≥99.0%, Sigma-Aldrich) and 1.725 g of $NH_4H_2PO_4$ (≥99.5%, Sigma-Aldrich) were in sequence dissolved into 60 mL of ultrapure water. Of note, each chemical was added into this solution before full dissolution of previous chemicals. The solution was then subjected to 80 °C with magnetic stirring for 5 h accompanied by a further drying treatment under a 120 °C vacuum oven for 24 h. Finally, the dried precursor was well ground after cooling down to room temperature and calcinated at 780 °C for 10 h under Ar flow (heating rate: 5 °C min^{-1}) to obtain HE-V. NVP was synthesized in the same method using 1.171 g of NH_4VO_3 without adding chemicals containing Cr/Mn/Fe/Al/Mg.

Physicochemical characterizations. All XRD results were obtained *via* a PANalytical Empyrean instrument (radiation: Cu K_α). The GSAS software was employed to conduct Rietveld refinements[1, 2]. The materials structures were depicted on a VESTA software[3]. A ThermoFisher ESCALAB 250Xi device (radiation: Al K_α) was carried out to collect XPS spectra. All XPS spectra were calibrated by C 1s (284.8 eV). The XPS peak seeking was hinged on the National Institute of Standards and Technology (NIST, USA) database. TGA was conducted in air at 10 °C min^{-1} on a STA 2500 Regulus apparatus. The materials microstructures were observed on Titan G2 60-300. Spectro Blue SOP was employed to get ICP results. FT-IR spectra were collected on Bruker Vertex 70. An electrolytic cell with a Be window was specially designed by Beijing SciStar technology Co., Ltd to collect the *in-situ* XRD patterns. The cycled electrodes were disassembled and were fully rinsed *via* dimethyl carbonate within a glove box prior to *ex-situ* measurements. XAS measurements were collected at 12-BM-B at the Advanced Photon Source (APS) in Argonne

National Laboratory. The radiation was monochromatized by a Si (111) double-crystal monochromator.

Electrochemical characterizations. 70% HE-V or NVP, 20% acetylene black and 10% polyvinylidene fluoride (gravimetric ratio) were dissolved in the N-methyl-2-pyrrolidone solvent. Afterwards, the wet slurry was pasted onto an Al foil *via* a doctor blade method. Then, the wet electrodes were subjected to an 80 °C vacuum oven for 12 h. All CR2032 coin cells were fabricated in an Ar glove box with Na metals as counter electrodes and GF/D (Whatman) glass fiber as separators. 1.0 mol L^{-1} $NaClO_4$ were dissolved in isovolumetric propylene carbonate and ethylene carbonate solvents with addition of 5 vol. % fluoroethylene carbonate as the electrolyte. All electrochemical tests and GITT were measured on a Neware battery test system (CT-4008T-5V10mA-164, Shenzhen, China). Five formation cycles were conducted before the GITT test. A Biologic VMP-3 electrochemical workstation was carried out to measure EIS (frequency range: 100 kHz to 0.01 Hz; amplitude: 10 mV) and CV results.

To ensure sufficient sodium inventory for full-cell operation and to enable activation of the full redox range of the HE-V cathode (including the low-voltage V^{3+}/V^{2+} couple at ~1.6 V), the commercial hard carbon (HC; KURARAY Co., Ltd., Japan) anodes were electrochemically presodiated prior to full-cell assembly. This was achieved by assembling HC electrodes into half-cells with sodium metal as the counter/reference electrode. The half-cells were cycled at 25 mA g^{-1} to a designated capacity corresponding to the targeted sodium inventory. After presodiation, the HC anodes were carefully retrieved, rinsed with dimethyl carbonate (DMC), dried, and then reassembled into full cells with HE-V cathodes under an argon atmosphere. As a result, the amount of pre-sodium could be calculated as 0.25 mg. The cathode mass loading was approximately 2.0 mg cm^{-2} (all batteries). To balance the capacity by controlling the cathode-to-anode active mass ratio, the anode mass loading was around 1.3 mg cm^{-2}. An N/P ratio of 1.1 was maintained based on the corresponding reversible capacities, and the applied current rate was referenced to the cathode.

Computational methods. All theoretical work was performed through utilizing the projector augmented wave approach within the DFT framework[4], as implemented in the Vienna *ab*-initio Simulation Package (VASP). The generalized gradient approximation (GGA) and Perdew–Burke–Ernzerhof (PBE) exchange functional[4] was conducted. The plane-wave energy cutoff was set to 500 eV, and the Monkhorst–Pack method[5] was carried out for the Brillouin zone sampling. The convergence criteria of energy and force calculations were set to 10^{-5} eV $atom^{-1}$ and 0.01 eV $Å^{-1}$, respectively. To consider the strong correlation effects of transition metal(s) in $Na_3V_2(PO_4)_3$ and $Na_{3.2}V_{1.5}Cr_{0.1}Mn_{0.1}Fe_{0.1}Al_{0.1}Mg_{0.1}(PO_4)_3$, both electronic structure calculations and structural optimizations were performed *via* using the spin-dependent GGA plus Hubbard correction U (GGA + U) method[6], and the effective U_{eff} parameters are 3.9 eV, 3.25 eV, 3.7 eV and 3.5 eV for Mn-3d, V-3d, Cr-3d and Fe-3d states[7], respectively. $Na_{3.2}V_{1.5}Cr_{0.1}Mn_{0.1}Fe_{0.1}Al_{0.1}Mg_{0.1}(PO_4)_3$ is built from $Na_3V_2(PO_4)_3$ with equal molar of V-Cr-Mn-Fe-Al-Mg mixing, i.e., V-Cr-Mn-Fe-Al-Mg cation arrangements in the V sites that were created within the 2×1×1 supercell of $Na_3V_2(PO_4)_3$ using the enumeration method[8] implemented in the Pymatgen code[9]. The V-Cr-Mn-Fe-Al-Mg cation arrangement of the most stable $Na_{3.2}V_{1.5}Cr_{0.1}Mn_{0.1}Fe_{0.1}Al_{0.1}Mg_{0.1}(PO_4)_3$ structure was determined by ranking the V-Cr-Mn-Fe-Al-Mg cation arrangements by their DFT energies. Moreover, determination of the stable structures of the sodium extracted compounds with Na-vacancy mixing were employed this same method. The energy barriers for Na diffusion in $Na_3V_2(PO_4)_3$ and $Na_{3.2}V_{1.5}Cr_{0.1}Mn_{0.1}Fe_{0.1}Al_{0.1}Mg_{0.1}(PO_4)_3$ were calculated by the nudged elastic band (NEB) method[10]. The crystal orbital Hamilton population (COHP) between neighboring oxygen ions were computed by the Lobster program[11], in which the negative and positive COHP values indicate bonding and anti-bonding, respectively. The pbeVaspFit2015 basis sets were used in the reconstruction of the PAW wave functions of each element.

The formation energy quantifies the thermodynamic stability of $Na_{3-x}V(PO_4)$ (or HE-V) relative to its constituent elements or reference phases. It is calculated for the partially desodiated phases ($x > 0$) to assess stability at different sodium contents, the formation energy (E_{form})of desodiation can be expressed as:

$$E_{\text{form}} = E_{\text{tot}}^{\mathrm{Na_{3-\mathit{x}}V(PO_4)}} - E_{\text{tot}}^{\mathrm{Na_3V(PO_4)}} + xE_{\text{tot}}^{\mathrm{Na}}$$

Where:

- $E_{\text{tot}}^{\mathrm{Na_3V(PO_4)}}$: DFT total energy of the pristine $\mathrm{Na_3V(PO_4)}$ per formula unit.
- $E_{\text{tot}}^{\mathrm{Na_{3-\mathit{x}}V(PO_4)}}$: DFT total energy of the desodiated phase.
- $E_{\text{tot}}^{\mathrm{Na}}$: DFT total energy of reference state (metallic Na).

The voltage of $Na_{3-x}V(PO_4)$ corresponds to the electrochemical potential for sodium deintercalation, derived from the Gibbs free energy change of the desodiation reaction. The average open-circuit voltage (OCV) is calculated between two sodium contents. The desodiation reaction for $Na_{3-x}V(PO_4)$ between sodium contents $\mathrm{x_1}$ and $\mathrm{x_2}$ $(\mathrm{x_1} > \mathrm{x_2})$ is:

$$\mathrm{Na}_{x_1}\mathrm{V(PO_4)} \rightarrow \mathrm{Na}_{x_2}\mathrm{V(PO_4)} + (x_1 - x_2)\mathrm{Na}$$

The Gibbs free energy change (ΔG) is approximated by the internal energy change (ΔE) at 0 K, neglecting entropy and volume terms (valid for solids):

$$\Delta E = E_{\text{tot}}^{\mathrm{Na}_{x_2}\mathrm{V(PO_4)}} - E_{\text{tot}}^{\mathrm{Na}_{x_1}\mathrm{V(PO_4)}} + (x_1 - x_2)E_{\text{tot}}^{\mathrm{Na}}$$

The average voltage is:

$$V = -\frac{\Delta E}{e(x_1 - x_2)}$$

Where:

- $E_{\text{tot}}^{\mathrm{Na}_{x_1}\mathrm{V(PO_4)}}$: DFT total energy of the phase with sodium content $\mathrm{x_1}$.
- $E_{\text{tot}}^{\mathrm{Na}_{x_2}\mathrm{V(PO_4)}}$: DFT total energy of the phase with sodium content $\mathrm{x_2}$.

- $E_{\text{tot}}^{\text{Na}}$: DFT total energy of metallic sodium (per atom).
- $x_1 - x_2$: Number of sodium ions removed.
- The negative sign ensures V is positive for a spontaneous electrochemical reaction.
- Units: ΔE in eV, and since 1 eV per electron corresponds to 1 V, the formula yields voltage in volts.

COMSOL Multiphysics simulation. The simulation was carried using the finite element method based on the COMSOL Multiphysics 6.2 platform, which mainly includes the electrochemical processes of HE-V and NVP cathodes. The model mainly reflects the difference of the sodium-ion transport capability between NVP and HE-V cathode in an electrochemical-mechanical coupled multi-physics field. The following are the details:[12]

The two main simulated electrochemical processes are charge transfer and ionic transport. Within the electrolyte, the transfer of ions is driven by the electric field and diffusion derived from concentration gradient, as described by the Nernst-Planck equation:

$$N_i = -D_{i,e}(\nabla c_{0,i} - \frac{z_i F c_{0,i}}{RT} \nabla \Phi)$$

Where N_i is flux, $D_{i,e}$, z_i and $c_{0,i}$ is the diffusion coefficient, charge and concentration of species *i* in the electrolyte, respectively. *F* is the Faraday's constant, *R* is the ideal gas constant, *T* is the Kelvin temperature and Φ is the electrolyte potential. Meanwhile, the ion in the electrolyte follows the equation of conservation of mass and charge:

$$\frac{\partial c_i}{\partial t} + \nabla \times N_i = 0$$

$$\sum_i z_i c_i = 0$$

Where c_i is the concentration, z_i is the valence of each species in the electrolyte. In the cathode active material particles, the mass transport is mainly controlled by diffusion, which is described by Fick's law:

$$N_i = -D_{i,s} \nabla c_{0,i}$$

Where $D_{i,s}$ is the diffusion coefficient in the active material particles. The charge transfer occurring at the interface between the anode and electrolyte, as well as the interface between the cathode particles and electrolyte, can be described as:

$$Na^{+} + e^{-} \leftrightarrow Na$$

Which is controlled by Butler-Volmer equation:

$$i_{loc} = i_{ex}\left[\exp\left(\frac{\alpha_a F\eta}{RT}\right) - \exp\left(\frac{-\alpha_c F\eta}{RT}\right)\right]$$

Where i_{loc} is the local current density, which could be used to quantify the local reaction rate. $\eta$is overpotential, α_a and α_c are the anodic and cathodic charge transfer coefficients, respectively, and i_{ex} is exchange current density which is highly related to the Li^{+} concentration gradient near the anode surface:

$$i_{ex} = i_e \prod_{i,v_j>0}\left(\frac{c_{Na^{+}}}{c_b}\right)^{\frac{\alpha_a v_j}{n_j}} \prod_{i,v_j<0}\left(\frac{c_{Na^{+}}}{c_b}\right)^{\frac{-\alpha_c v_j}{n_j}}$$

Where $c_{Na^{+}}$ and c_b are the concentration of Na^{+} near the anode and in the bulk electrolyte, respectively; i_e is the current density to represent the kinetics of electrons, v_j is the stoichiometric coefficients, n_j is the number of electrons transferred. Both the anodic and cathodic charge transfer coefficients are set as 0.5.

Supplementary Figures and Tables

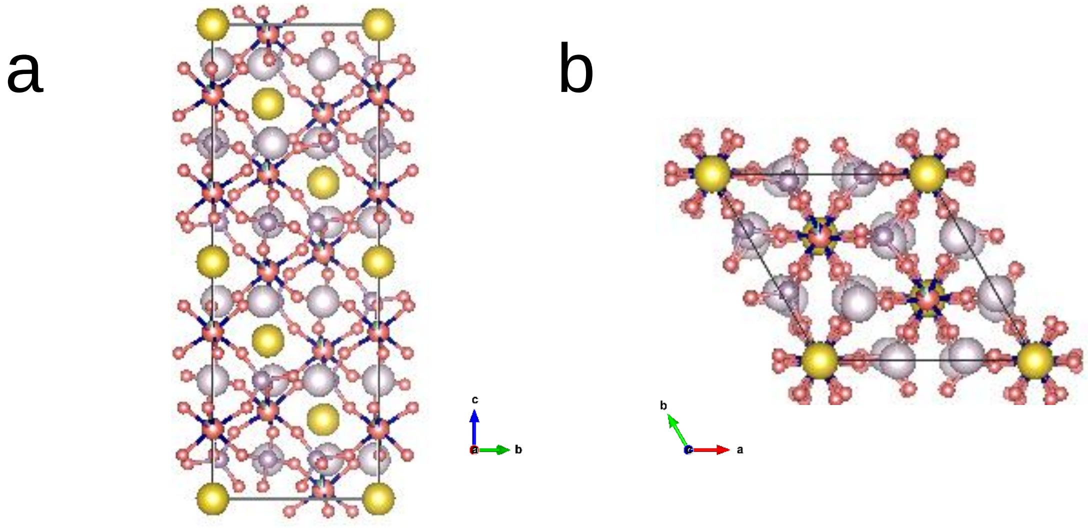

Figure S1. Illustrations of crystalline structure of HE-V.

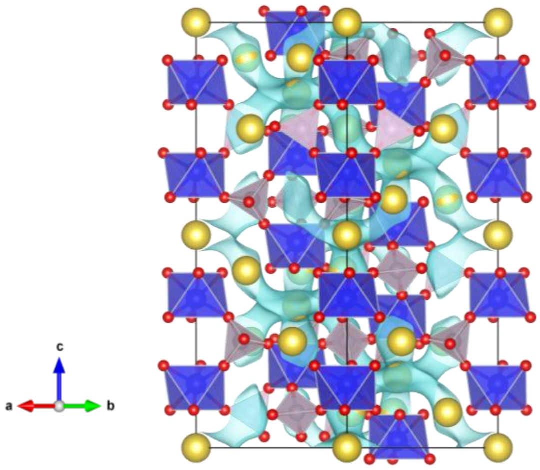

Figure S2. BV map of Na^{+} ions in NVP (the isosurface value is 0.5 e $Å^{-3}$).

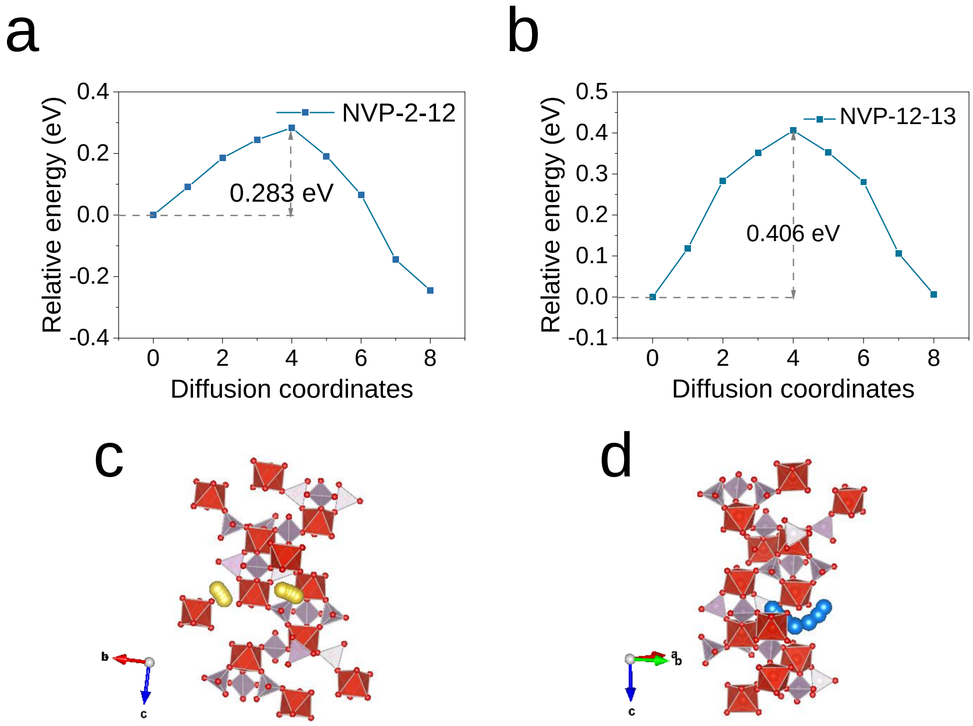

Figure S3. Na^+ ion migration channels and the corresponding migration energy barriers of NVP. V-2-12 represents the pathway of Na^+ around the V atom from Na2 to Na12.

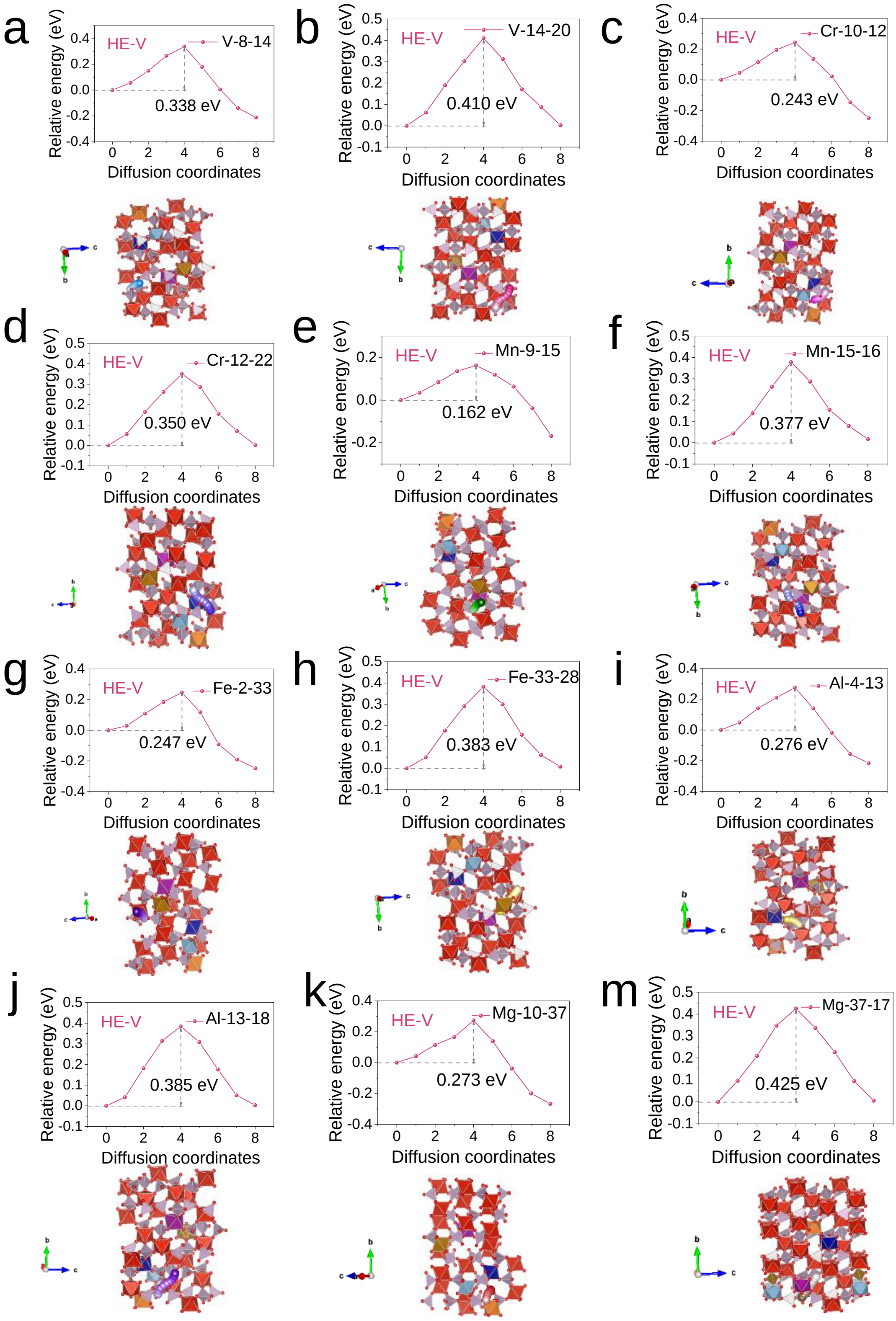

Figure S4. Na$^+$ ion migration channels and the corresponding migration energy barriers of HE-V. e.g., V-8-14 represents the pathway of Na$^+$ around the V atom from Na8 to Na14.

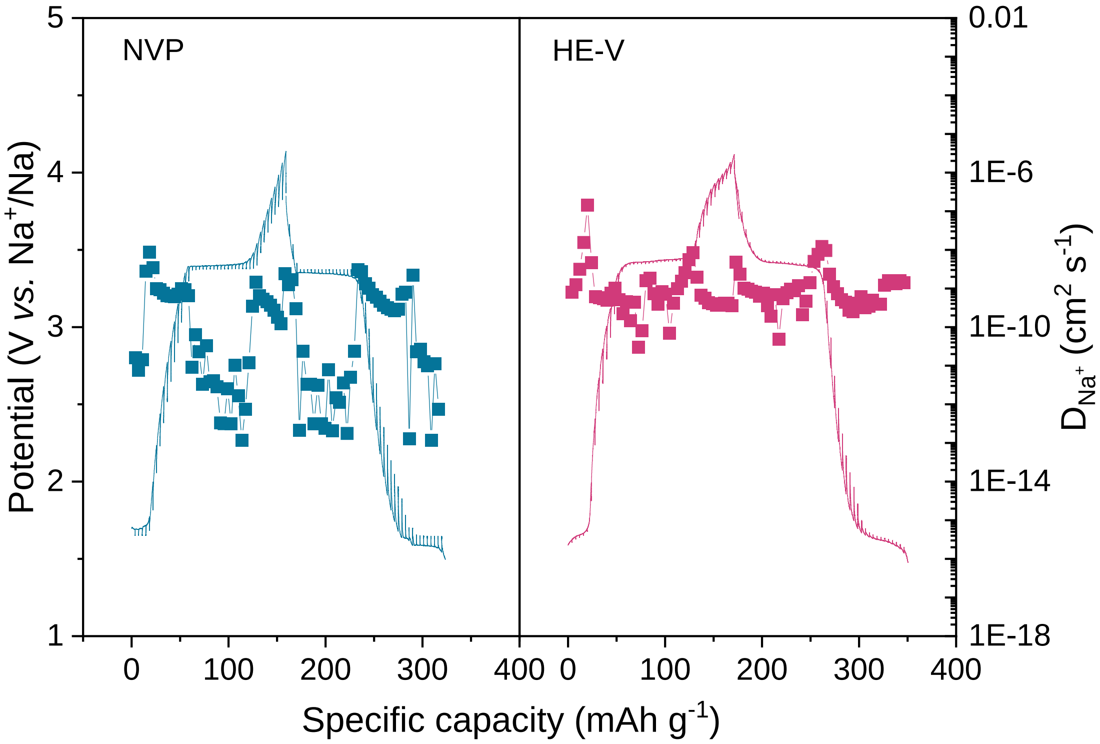

Figure S5. Galvanostatic intermittent titration technique (GITT) profiles and the Log (D_{Na+})-Capacity plots of NVP and HE-V during charge/discharge processes.

*Note: GITT measurements were conducted to evaluate Na^+ diffusion coefficients across the voltage range. The HE-V sample exhibited consistently higher diffusion coefficients compared to NVP, indicating enhanced ionic conductivity and more efficient Na^+ transport kinetics.

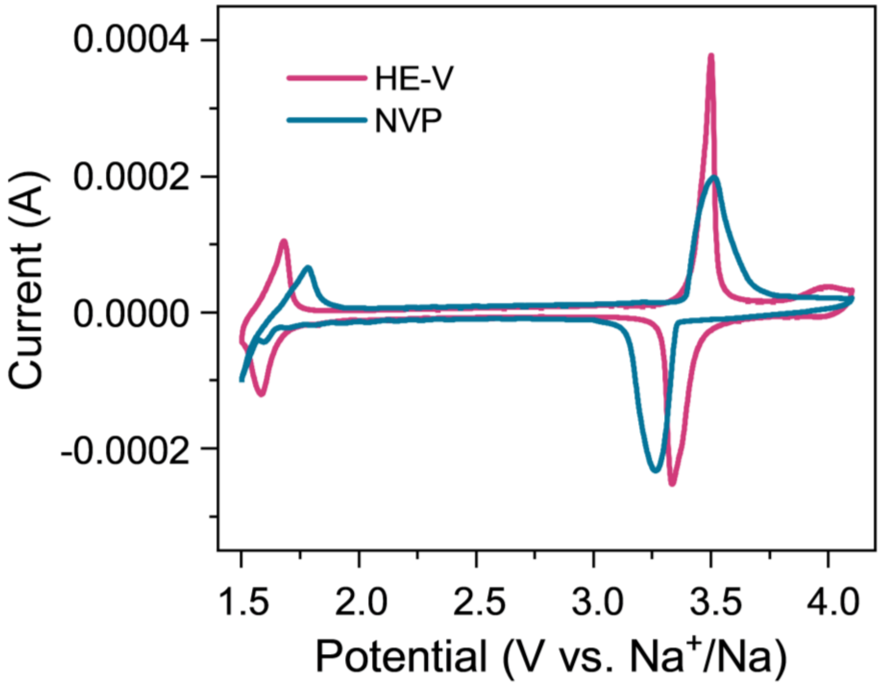

Figure S6. Cyclic voltammetry (CV) curves of NVP and HE-V recorded at a scan rate of 0.1 mV s^{-1}.

*Note: CV curves of NVP and HE-V at a scan rate of 0.1 mV s^{-1} were analyzed to evaluate redox kinetics and Na^+ diffusion behavior. HE-V exhibits a markedly higher response current, larger peak area, and a narrower potential gap between cathodic and anodic peaks, indicating superior redox kinetics and enhanced Na^+ diffusion compared to NVP.

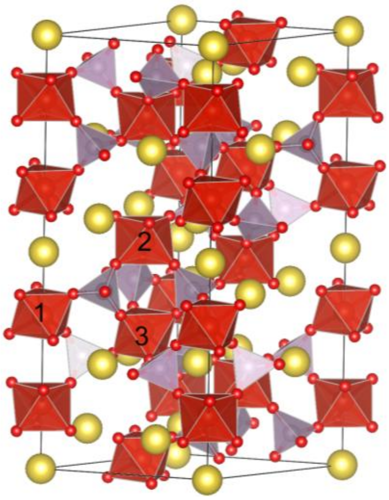

Figure S7. Crystal structure model for COHP and ICOHP of both HE-V and NVP. The noted number represents that there are three different types of V in each sample.

Table S1. Integrated crystal orbital Hamilton population (ICOHP) of V-O bonds (first-type V) in HE-V.

Type of bond	Spin direction	ICOHP (eV/bond)
V50-O109	Spin up	-0.54
	Spin down	-0.62
V50-O133	Spin up	-0.62
	Spin down	-0.65
V50-O157	Spin up	-0.61
	Spin down	-0.68
V50-O181	Spin up	-0.60
	Spin down	-0.63
V50-O205	Spin up	-0.56
	Spin down	-0.61
V50-O229	Spin up	-0.56
	Spin down	-0.60
Integral ICOHP (eV)		-7.28

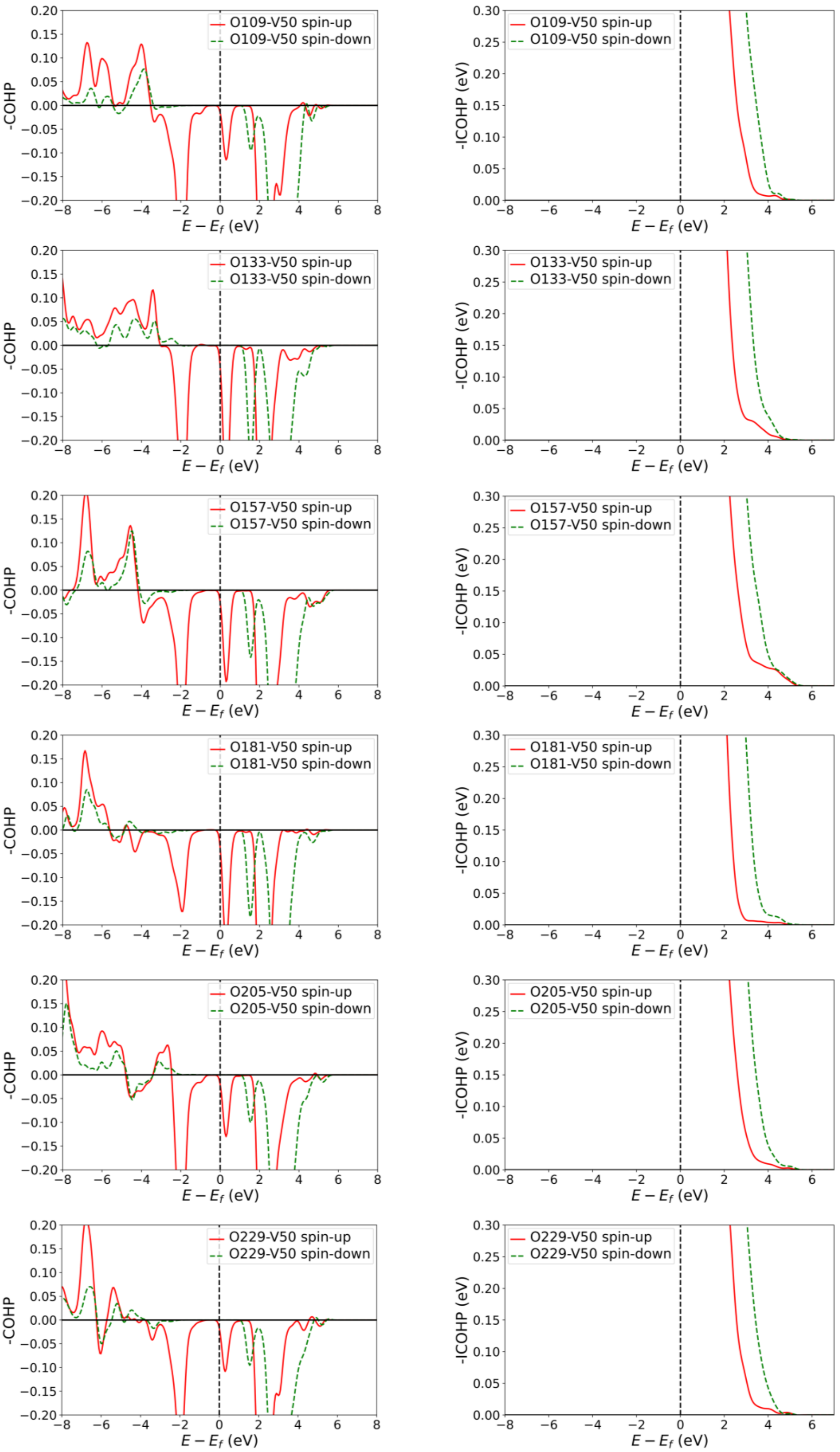

Figure S8. COHP and ICOHP results of V50 atom (first-type V) interacting with different O atoms around it in HE-V.

Table S2. Integrated crystal orbital Hamilton population (ICOHP) of V-O bonds (second-type V) in HE-V.

Type of bond	**Spin direction**	**ICOHP (eV/bond)**
V52-O111	Spin up	-0.55
	Spin down	-0.60
V52-O135	Spin up	-0.59
	Spin down	-0.64
V52-O159	Spin up	-0.54
	Spin down	-0.61
V52-O183	Spin up	-0.57
	Spin down	-0.61
V52-O207	Spin up	-0.54
	Spin down	-0.59
V52-O231	Spin up	-0.55
	Spin down	-0.60
Integral ICOHP (eV)		-6.99

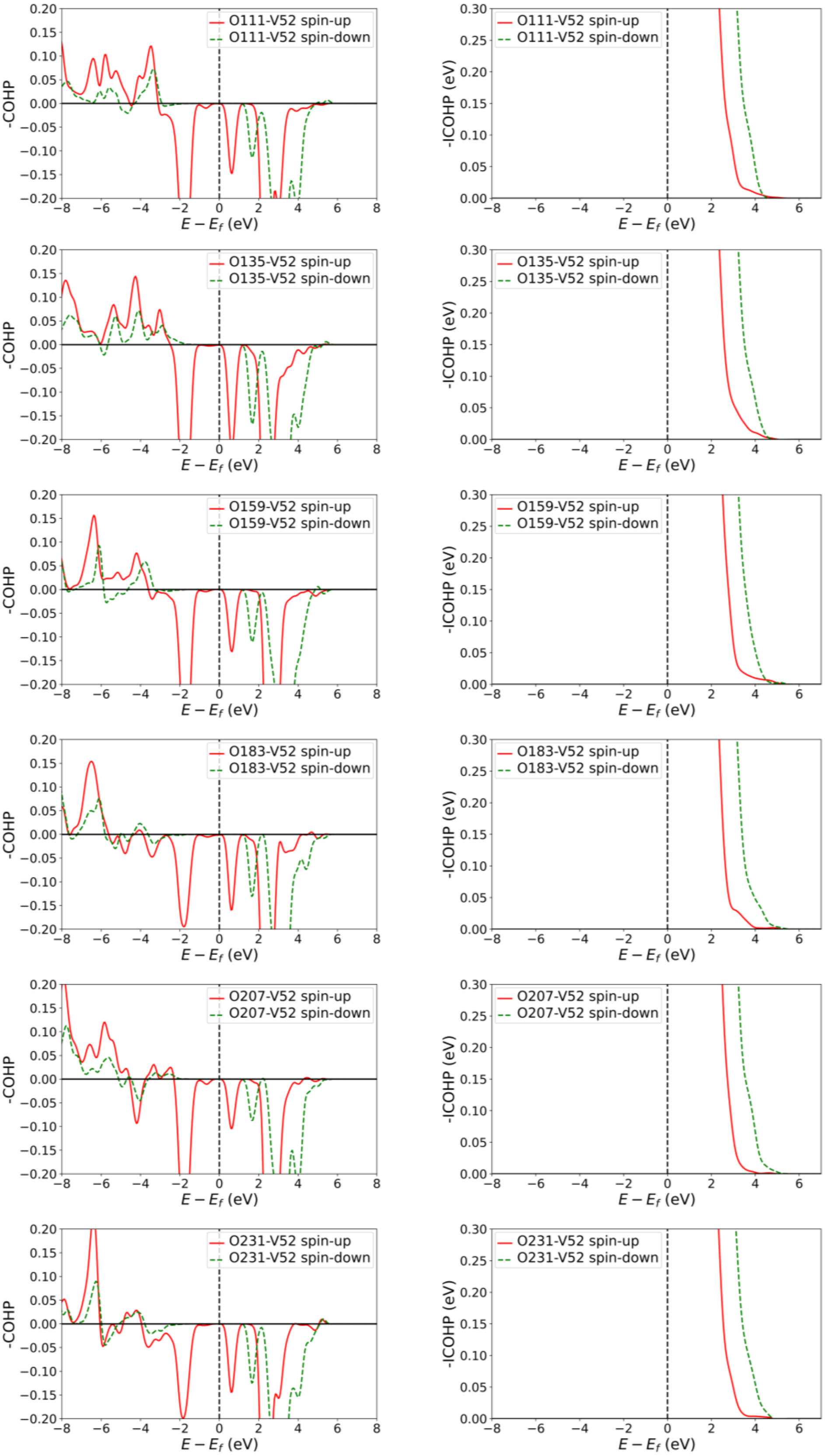

Figure S9. COHP and ICOHP results of V52 atom (second-type V) interacting with different O atoms around it in HE-V.

Table S3. Integrated crystal orbital Hamilton population (ICOHP) of V-O bonds (third-type V) in HE-V.

Type of bond	Spin direction	ICOHP (eV/bond)
V57-O116	Spin up	-0.49
	Spin down	-0.51
V57-O140	Spin up	-0.54
	Spin down	-0.53
V57-O164	Spin up	-0.46
	Spin down	-0.51
V57-O188	Spin up	-0.53
	Spin down	-0.51
V57-O212	Spin up	-0.49
	Spin down	-0.48
V57-O236	Spin up	-0.54
	Spin down	-0.53
Integral ICOHP (eV)		-6.12

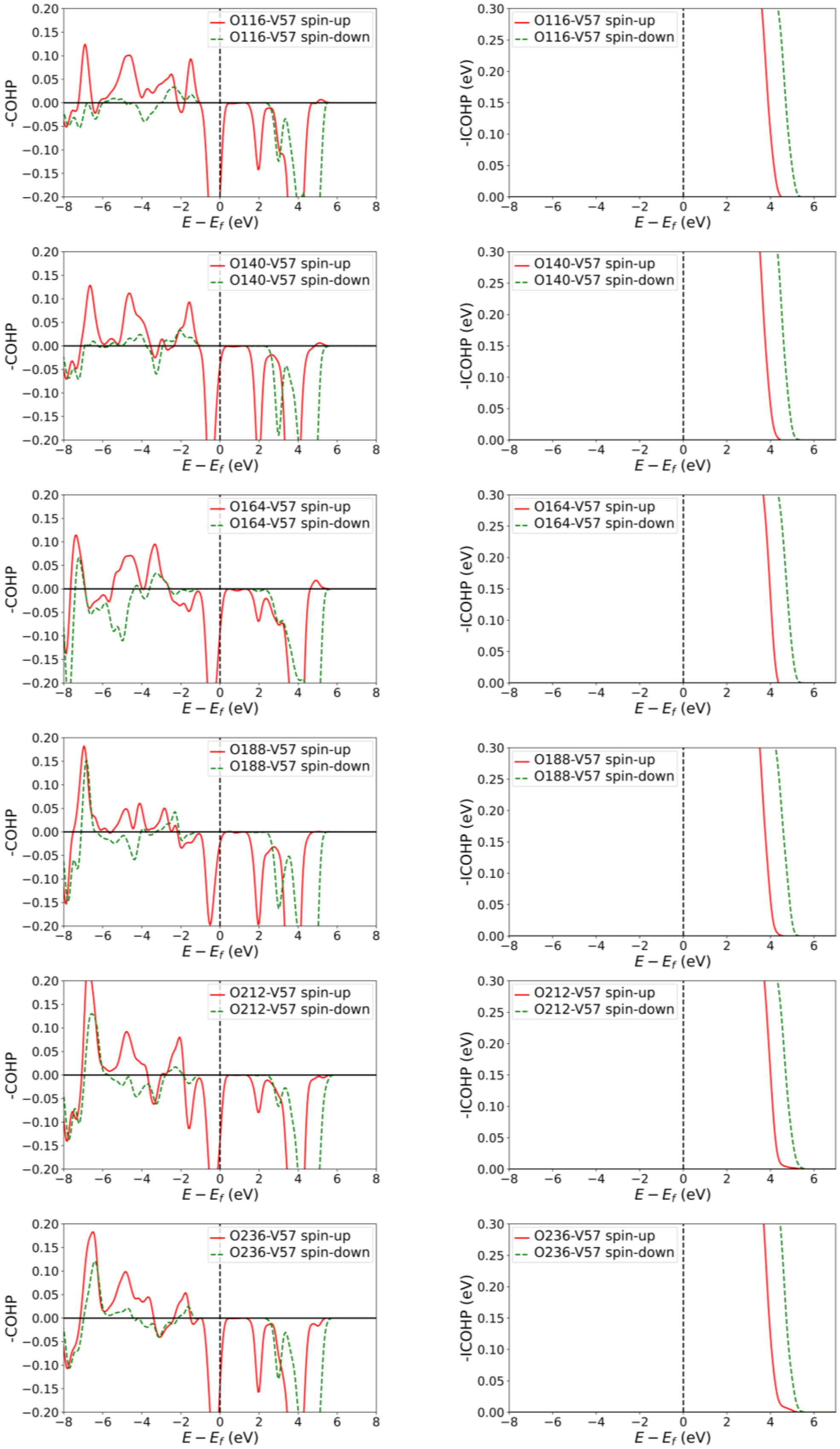

Figure S10. COHP and ICOHP results of V57 atom (third-type V) interacting with different O atoms around it in HE-V.

Table S4. Integrated crystal orbital Hamilton population (ICOHP) of V-O bonds (first-type V) in NVP.

Type of bond	**Spin direction**	**ICOHP (eV/bond)**
V26-O72	Spin up	-0.55
	Spin down	-0.61
V26-O74	Spin up	-0.51
	Spin down	-0.55
V26-O76	Spin up	-0.49
	Spin down	-0.55
V26-O108	Spin up	-0.45
	Spin down	-0.48
V26-O110	Spin up	-0.45
	Spin down	-0.49
V26-O112	Spin up	-0.41
	Spin down	-0.43
Integral ICOHP (eV)		-5.97

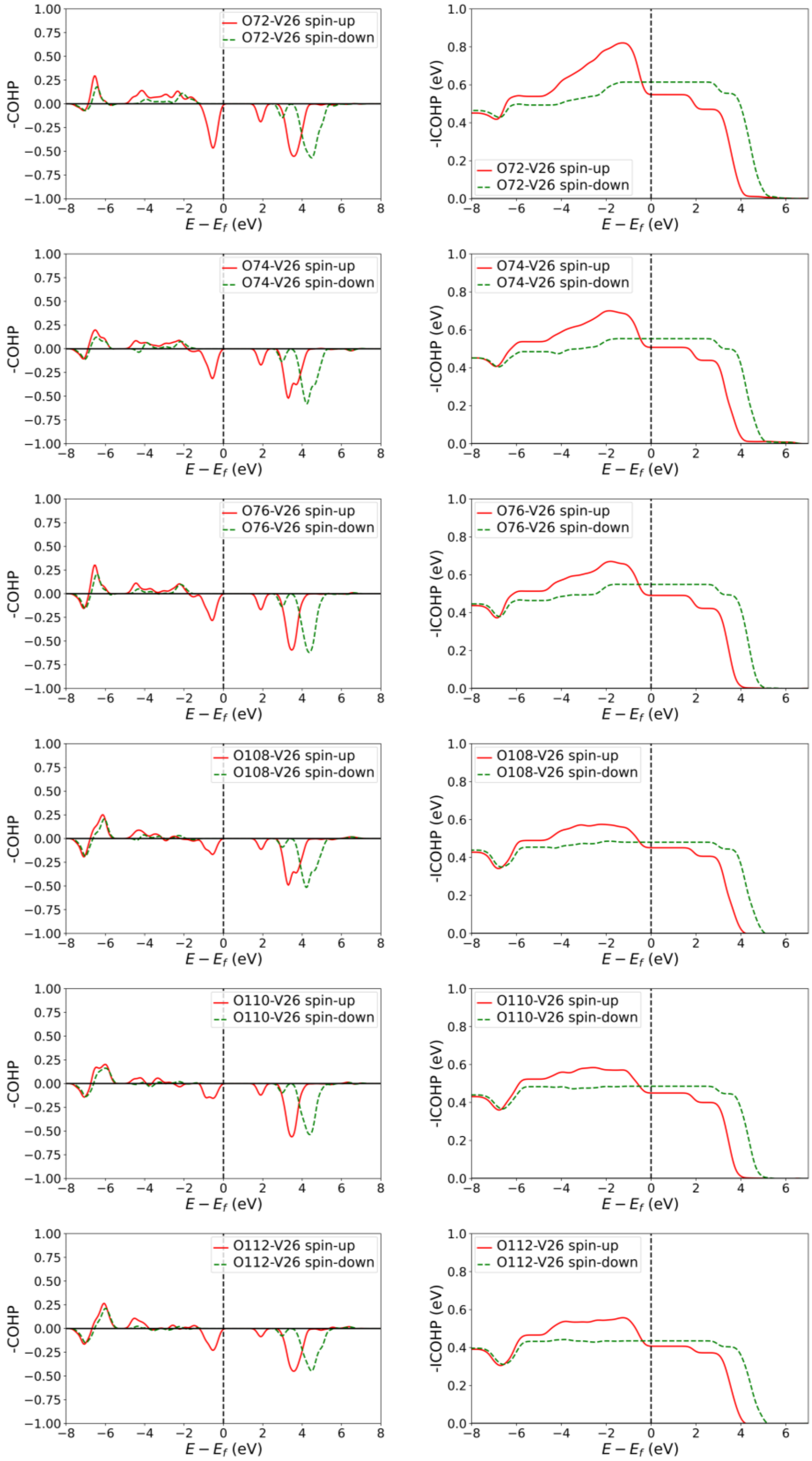

Figure S11. COHP and ICOHP results of V26 atom (first-type V) interacting with different O atoms around it in NVP.

Table S5. Integrated crystal orbital Hamilton population (ICOHP) of V-O bonds (second-type V) in NVP.

Type of bond	Spin direction	ICOHP (eV/bond)
V27-O73	Spin up	-0.56
	Spin down	-0.63
V27-O75	Spin up	-0.50
	Spin down	-0.55
V27-O77	Spin up	-0.50
	Spin down	-0.55
V27-O109	Spin up	-0.46
	Spin down	-0.49
V27-O111	Spin up	-0.44
	Spin down	-0.47
V27-O113	Spin up	-0.41
	Spin down	-0.44
Integral ICOHP (eV)		-6

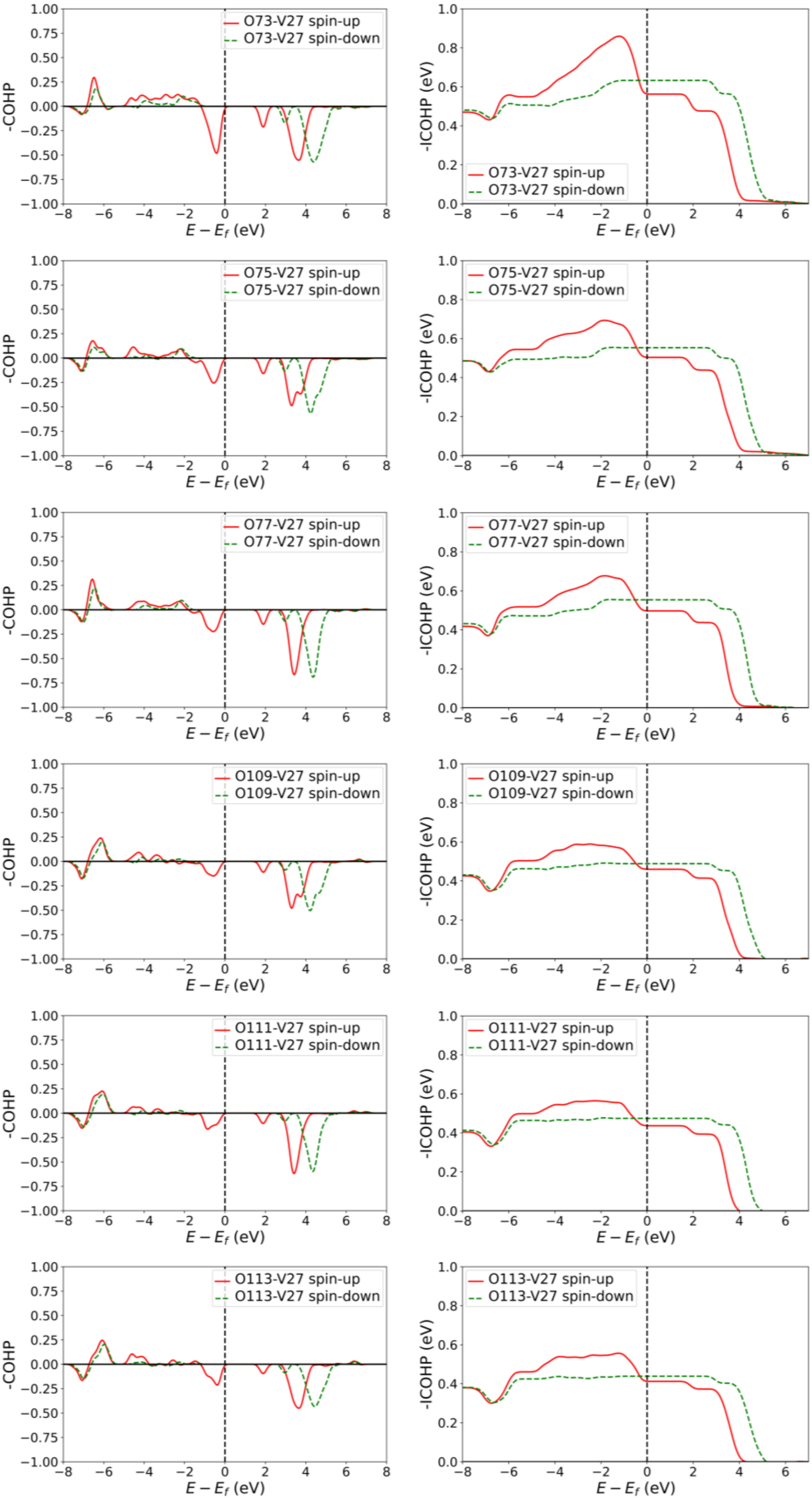

Figure S12. COHP and ICOHP results of V27 atom (second-type V) interacting with different O atoms around it in NVP.

Table S6. Integrated crystal orbital Hamilton population (ICOHP) of V-O bonds (third-type V) in NVP.

Type of bond	**Spin direction**	**ICOHP (eV/bond)**
V29-O79	Spin up	-0.49
	Spin down	-0.55
V29-O81	Spin up	-0.55
	Spin down	-0.62
V29-O83	Spin up	-0.50
	Spin down	-0.56
V29-O115	Spin up	-0.42
	Spin down	-0.45
V29-O117	Spin up	-0.45
	Spin down	-0.48
V29-O119	Spin up	-0.46
	Spin down	-0.49
Integral ICOHP (eV)		-6.02

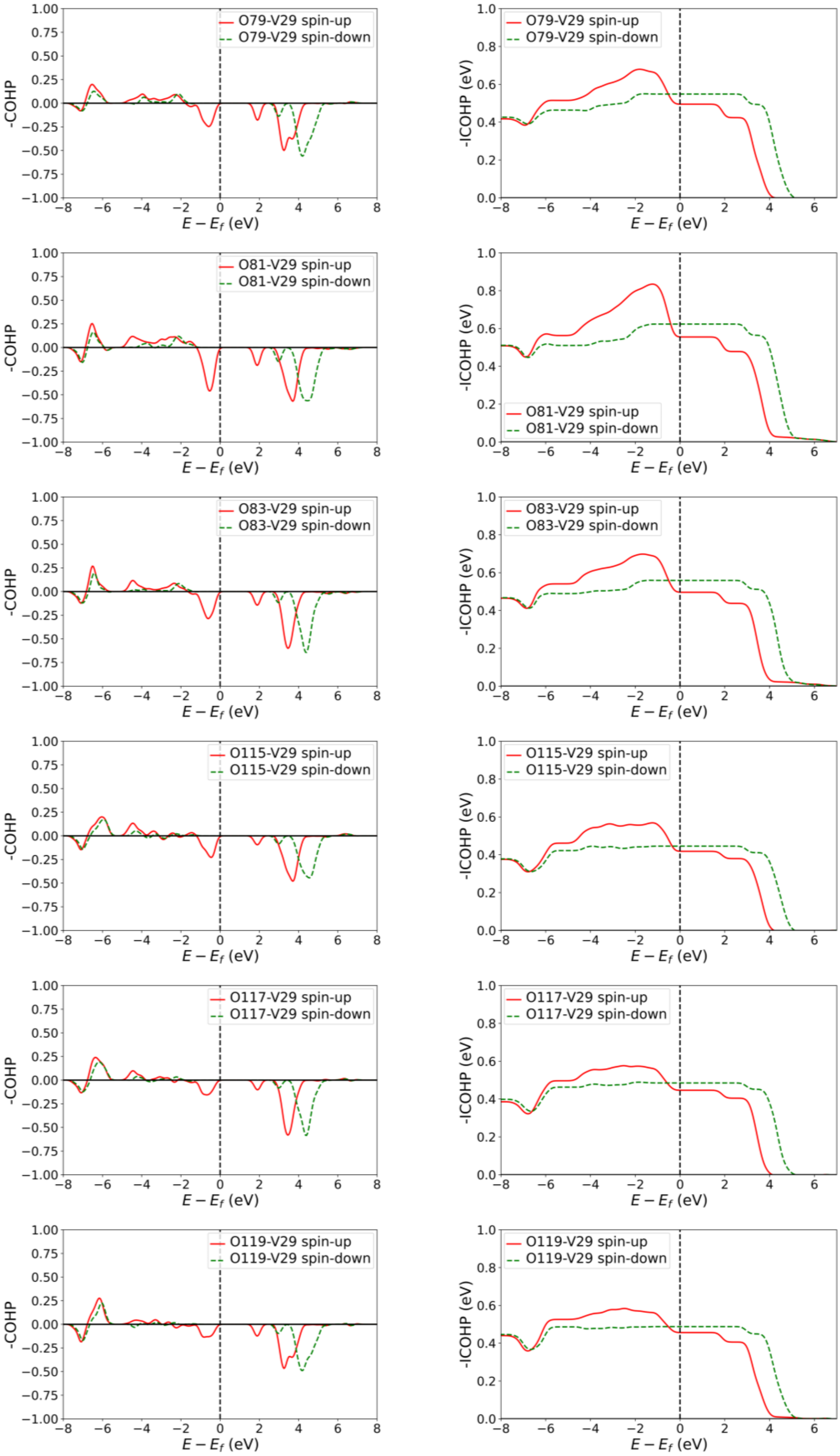

Figure S13. COHP and ICOHP results of V29 atom (third-type V) interacting with different O atoms around it in NVP.

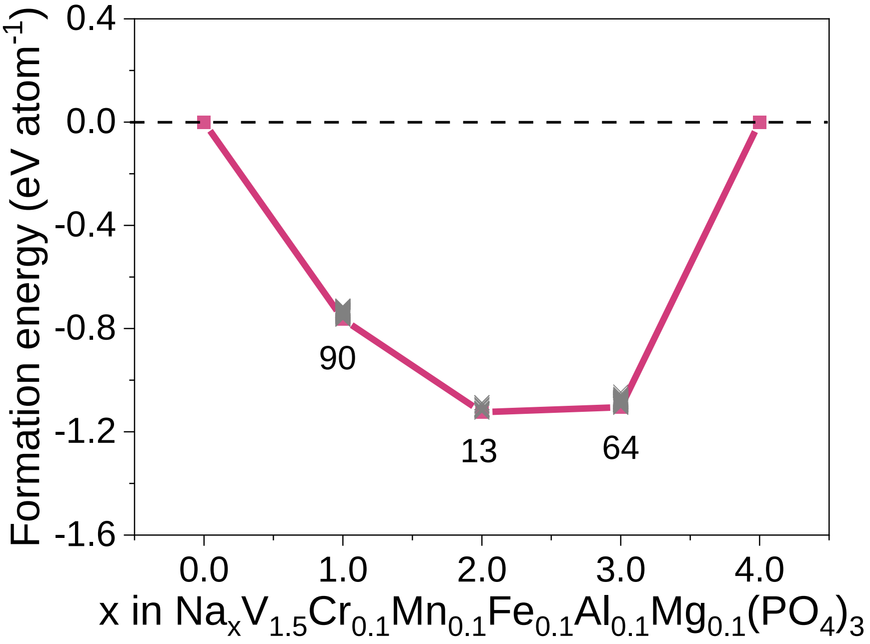

Figure S14. Convex-hull phase diagram of HE-V.

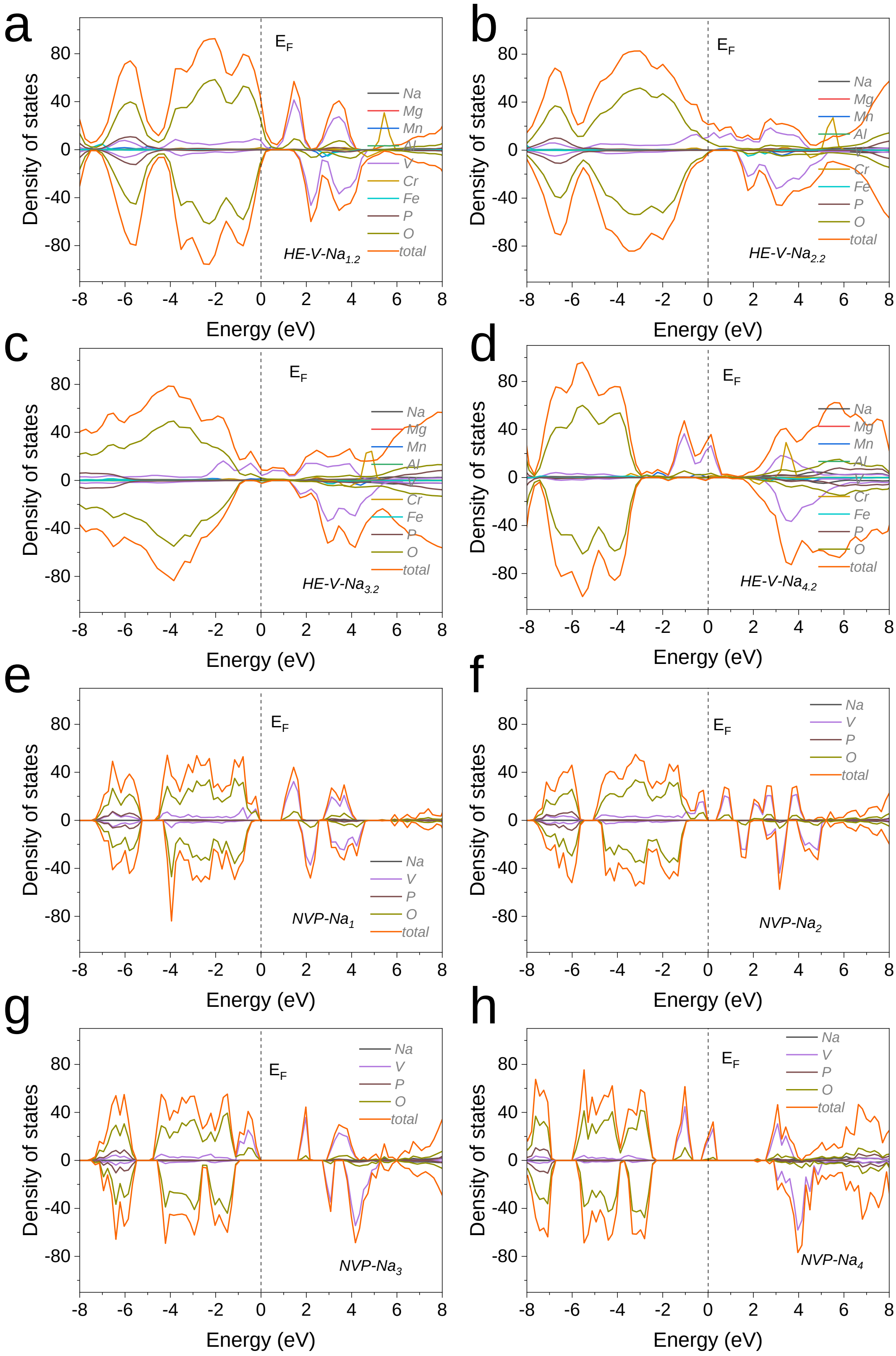

Figure S15. DOS patterns of (a-d) HE-V and (e-h) NVP with different Na contents.

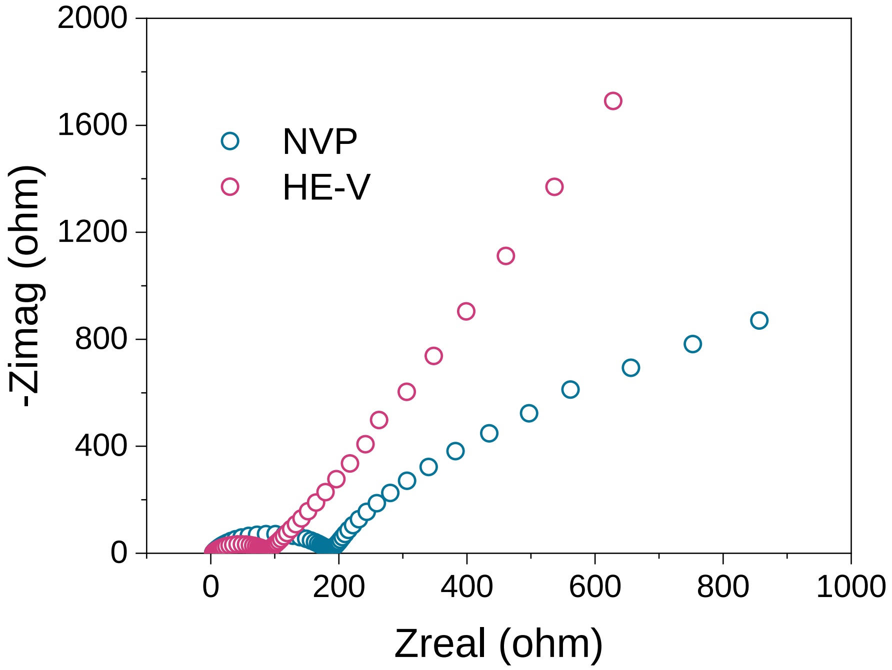

Figure S16. EIS results of HE-V and NVP.

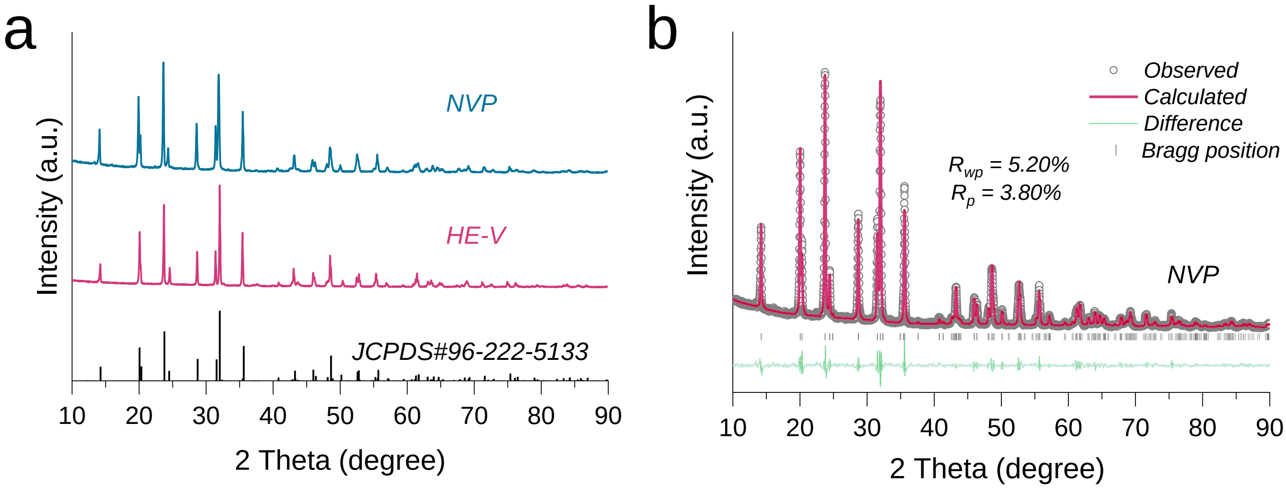

Figure S17. a XRD comparison and **b** the corresponding Rietveld refinement for NVP.

Table S7. Detailed structural information of HE-V derived from Rietveld refinement.

Space group = $R\bar{3}c$	R_{wp} = 3.41%	R_p = 2.45%
a (Å) = 8.77(3)	c (Å) = 21.72(6)	α (°) = 90
β (°) = 90	γ (°) = 120	V (Å^3) = 1448.23(5)

Atom	x	y	z	frac	site
Na1	0.0000(0)	0.0000(0)	0.0000(0)	1.03(0)	6b
Na2	0.6391(7)	0.0000(0)	0.2500(0)	0.97(1)	18e
V	0.0000(0)	0.0000(0)	0.1473(4)	0.75(0)	12c
Cr	0.0000(0)	0.0000(0)	0.1473(4)	0.05(0)	12c
Mn	0.0000(0)	0.0000(0)	0.1473(4)	0.05(0)	12c
Fe	0.0000(0)	0.0000(0)	0.1473(4)	0.05(0)	12c
Al	0.0000(0)	0.0000(0)	0.1473(4)	0.05(0)	12c
Mg	0.0000(0)	0.0000(0)	0.1473(4)	0.05(0)	12c
P	0.2948(5)	0.0000(0)	0.2500(0)	1.00(0)	18e
O1	0.0297(6)	0.2054(2)	0.1926(0)	1.00(0)	36f
O2	0.1819(8)	0.1744(5)	0.0926(2)	1.00(0)	36f

Table S8. Detailed structural information of NVP derived from Rietveld refinement.

Space group = R$\bar{3}$c		R_{wp} = 5.20%		R_p = 3.80%	
a (Å) = 8.73(0)		c (Å) = 21.82(8)		α (°) = 90	
β (°) = 90		γ (°) = 120		V (Å^3) = 1440.75(1)	
Atom	x	y	z	frac	site
Na1	0.3333(3)	0.6666(7)	0.1666(7)	0.80(5)	6b
Na2	0.6666(7)	0.9180(5)	0.0833(3)	0.73(1)	18e
V	0.3333(3)	0.6666(7)	0.0142(3)	1.00(0)	12c
P	0.0132(0)	0.3333(3)	0.0833(3)	1.00(0)	18e
O1	0.1218(9)	0.5103(0)	0.0879(0)	1.00(0)	36f
O2	0.5226(4)	0.7949(9)	0.0297(9)	1.00(0)	36f

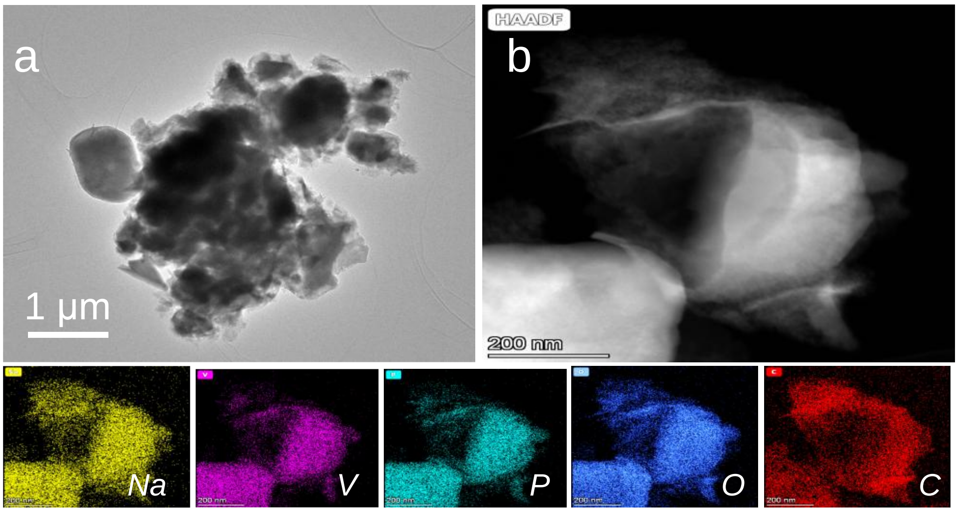

Figure S18. (a) TEM image and **(b)** EDS mapping images of NVP.

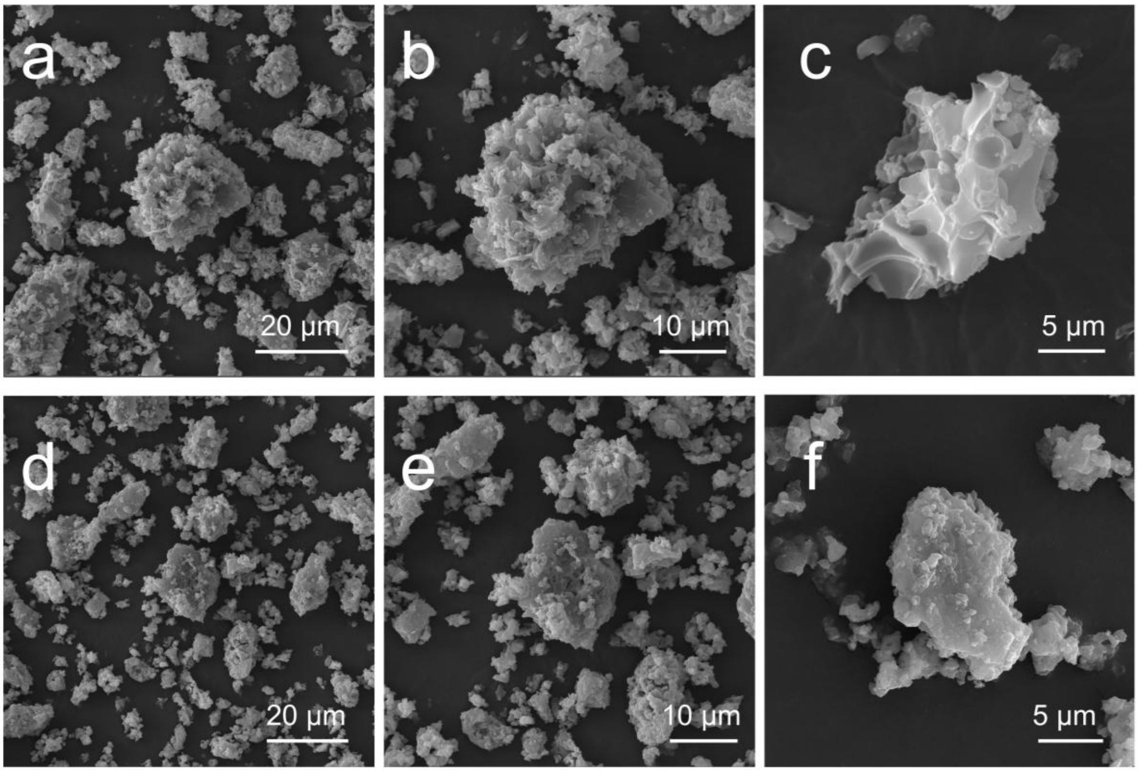

Figure S19. SEM images of (a-c) NVP and (d-f) HE-V.

*Note: it can be clearly observed from SEM images in Figure S19a-c that NVP appears an irregular morphology and the micron particles. When introducing dopants into NVP, HE-V presents apparent hierarchical structure of various nanoparticles (Fig. S19d-f), which are relatively smaller than those of NVP. Furthermore, both samples display a relatively smooth surface except that they are covered by some small particles.

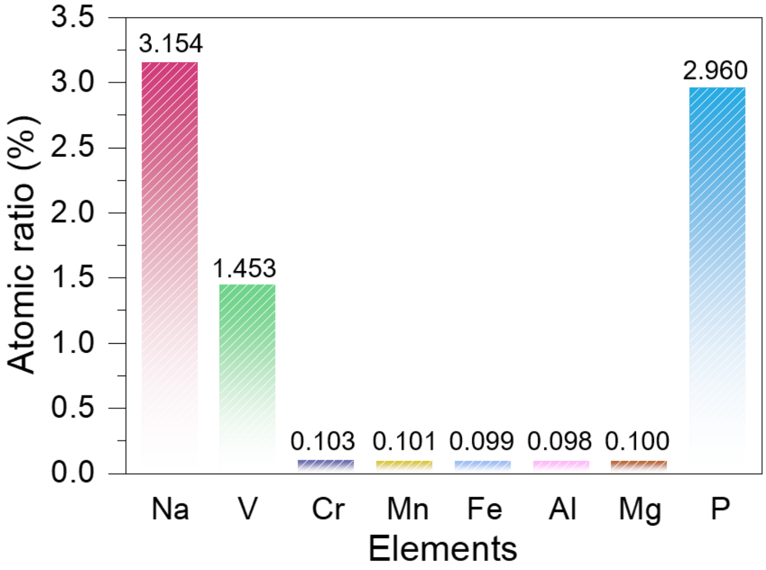

Figure S20. ICP-OES results of HE-V.

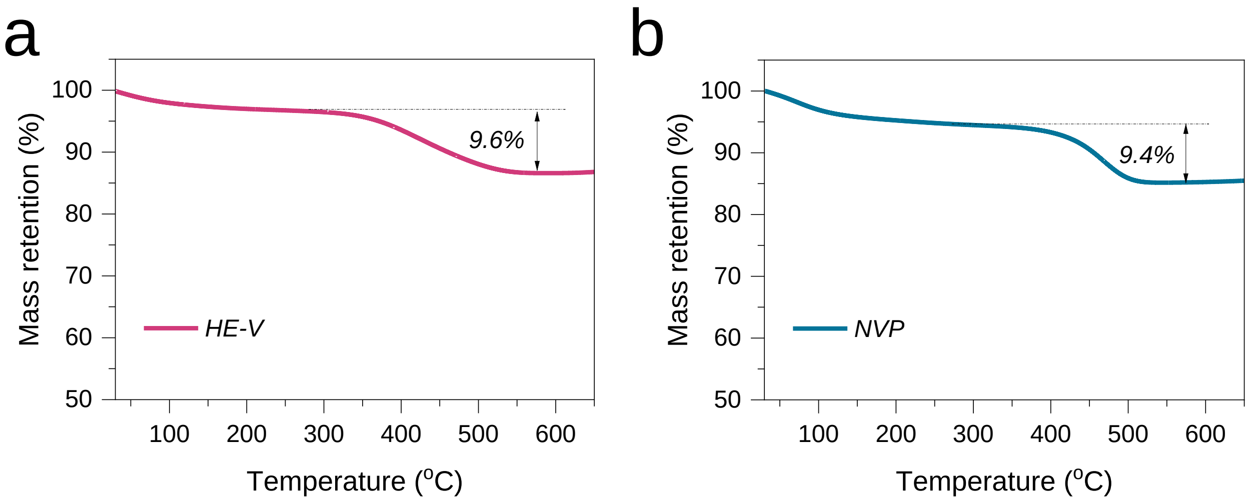

Figure S21. TGA results of (a) HE-V and (b) NVP.

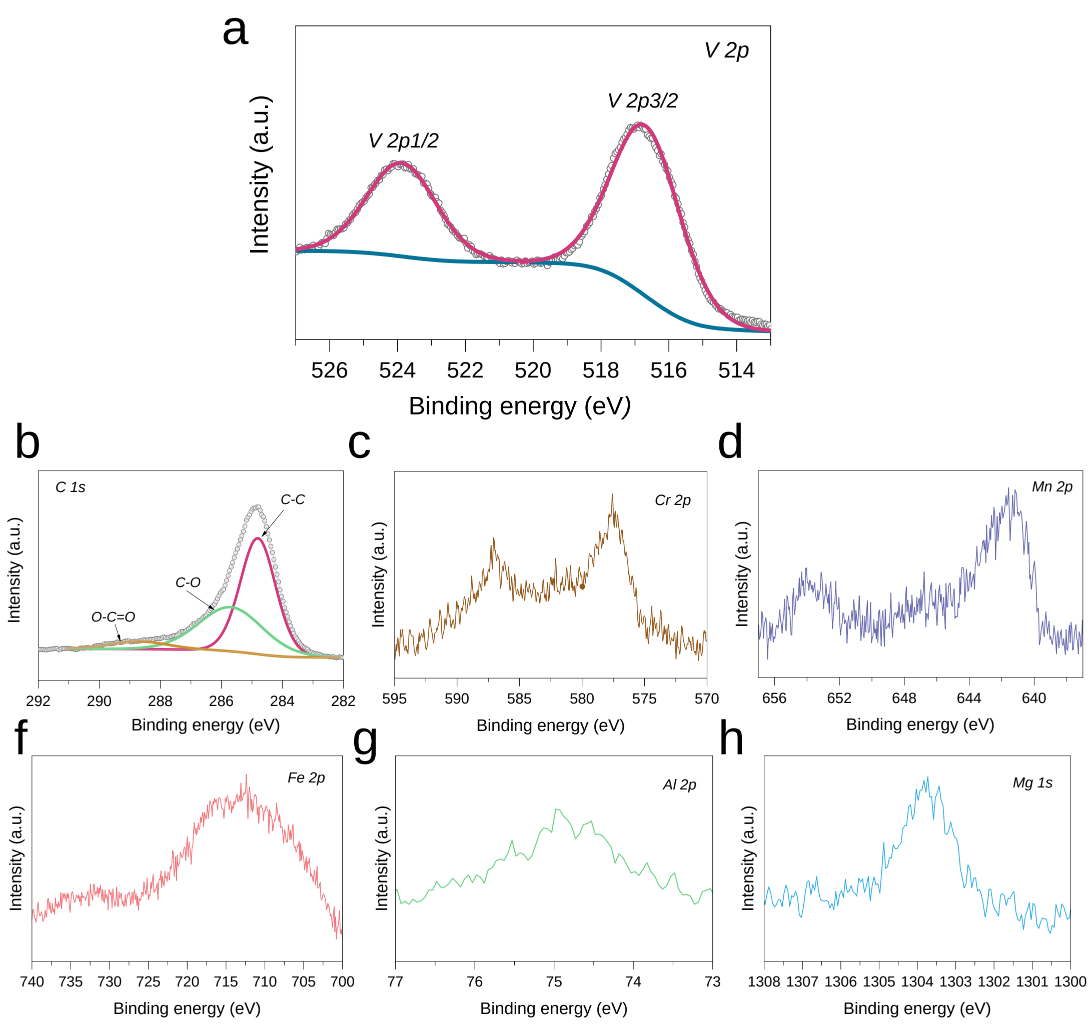

Figure S22. XPS spectra of HE-V.

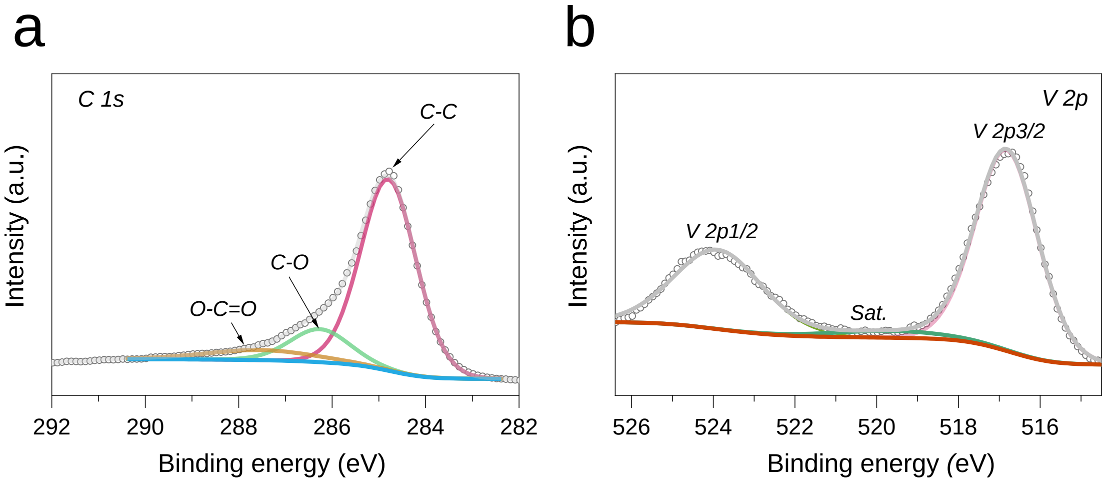

Figure S23. XPS spectra of NVP.

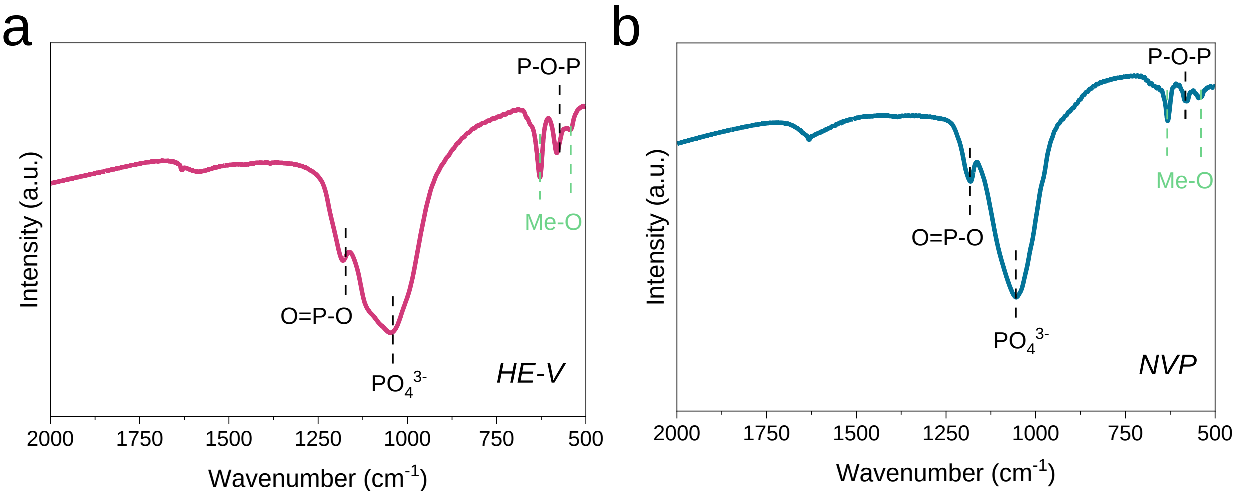

Figure S24. FT-IR results of (a) HE-V and (b) NVP.

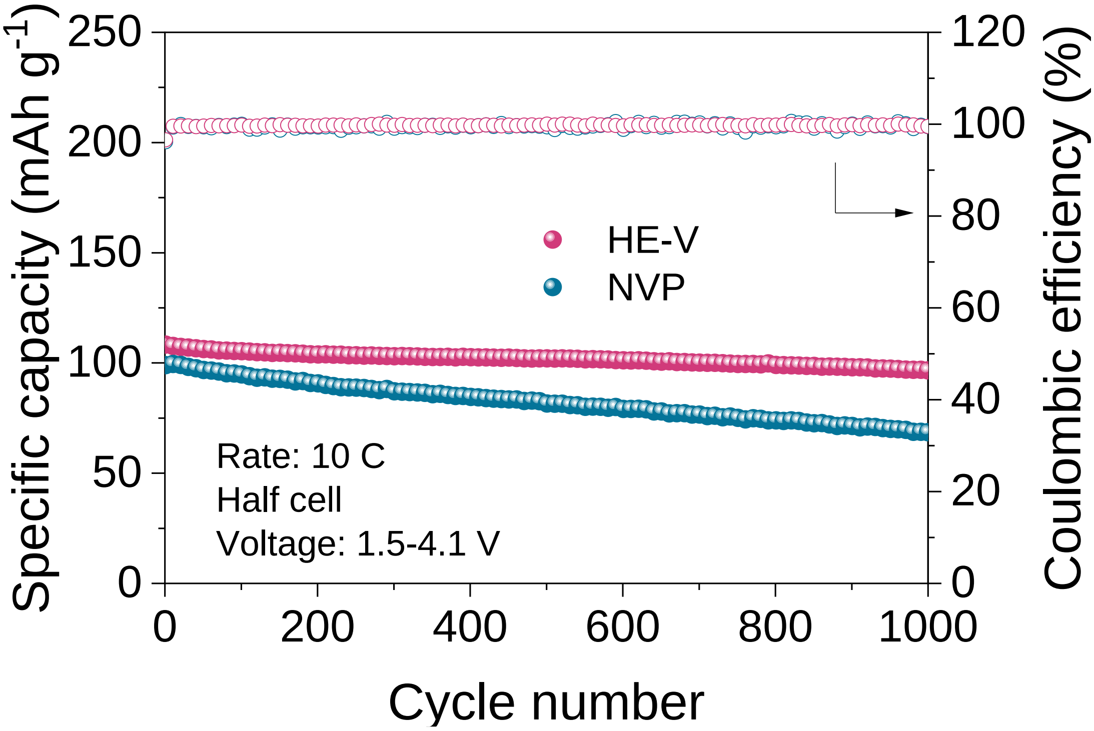

Figure S25. Cycling performance of NVP at 10 C.

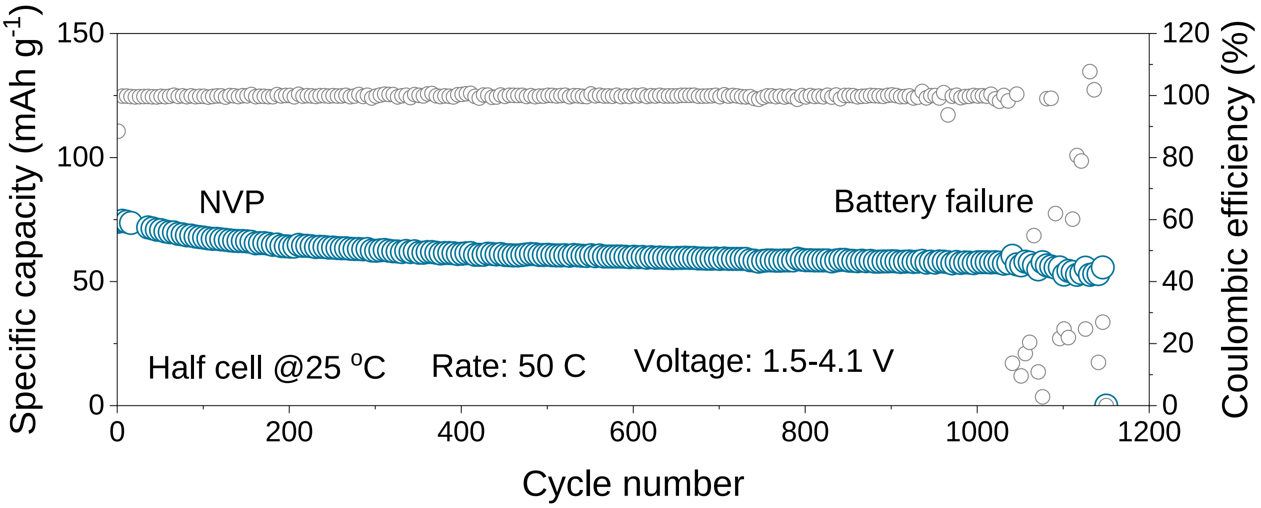

Figure S26. Cycling performance of NVP at 50 C.

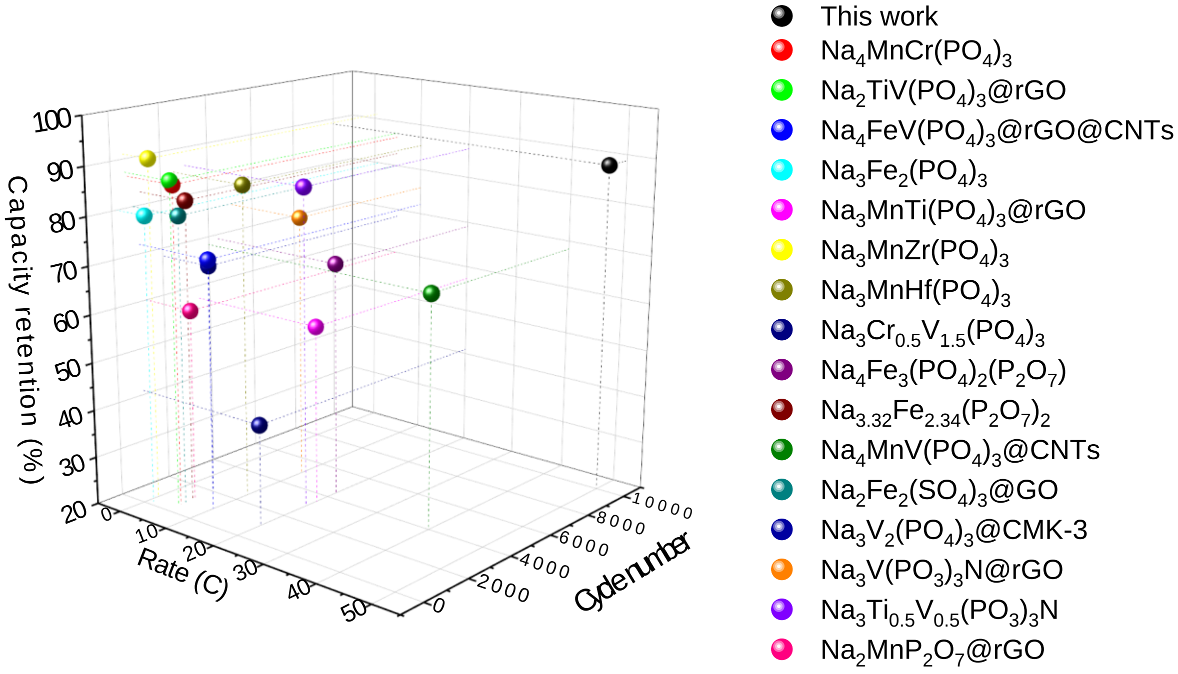

Figure S27. Comparison of capacity retention during cycling between this work and previously reported polyanionic Na-storage cathodes.

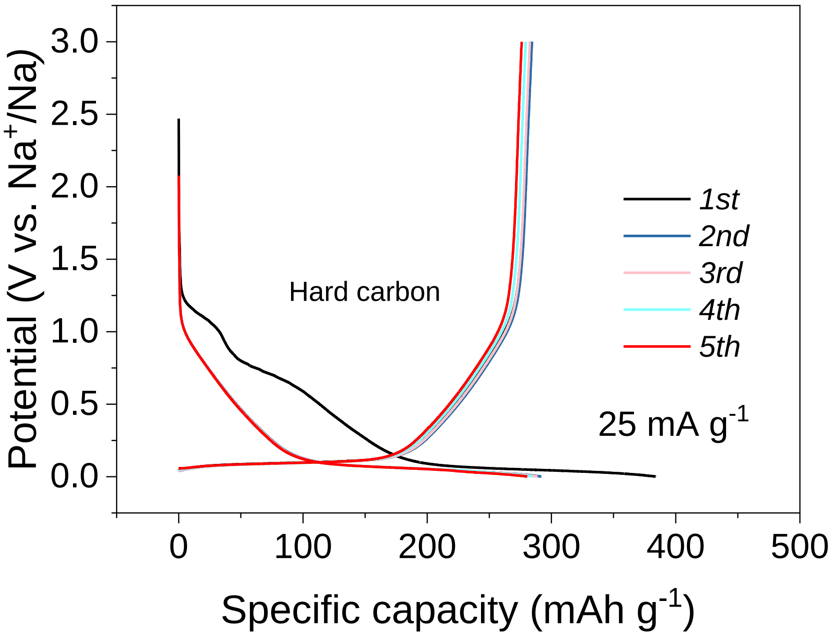

Figure S28. Galvanostatic charge/discharge curves of the hard carbon anode for initial first 5 cycles at 25 mA g^{-1}.

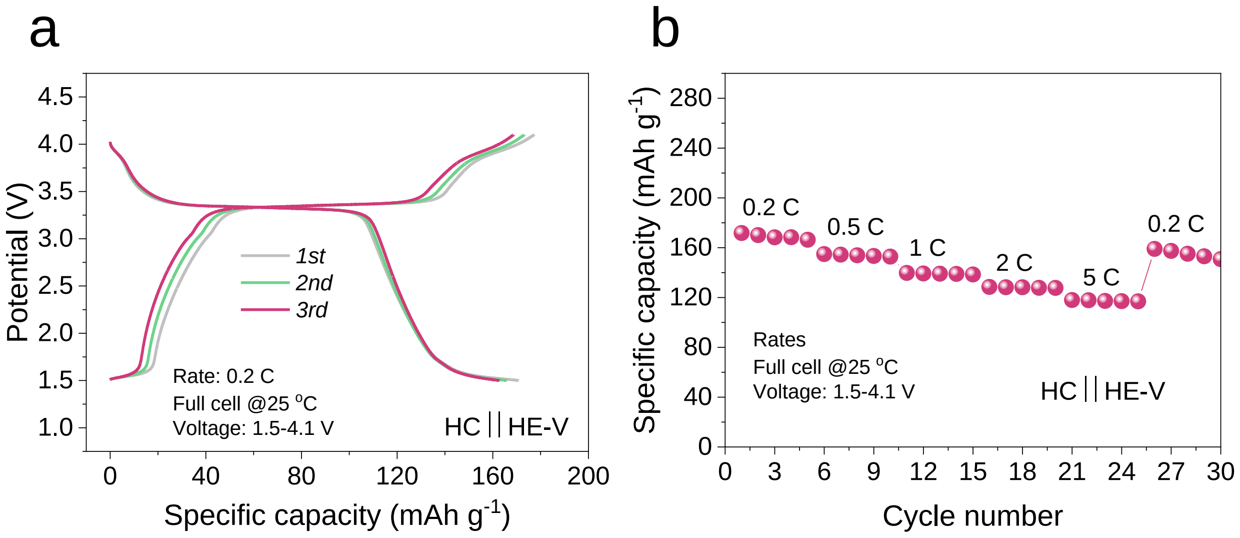

Figure S29 (a) Initial three charge/discharge curve at 0.2 C and (b) rate capability of the HC‖HE-V full cell.

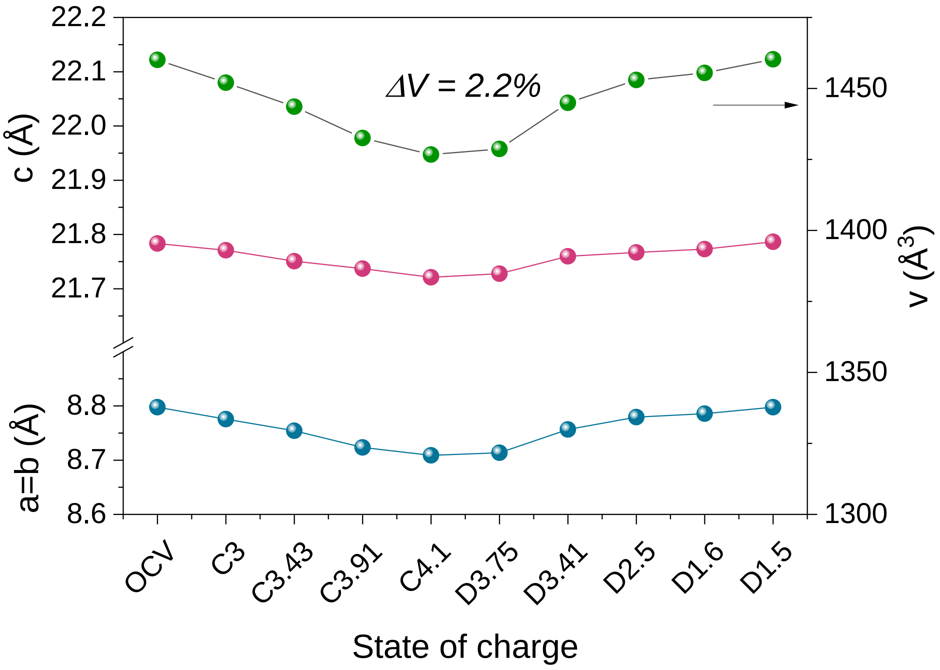

Figure S30. Changes of the lattice parameters of HE-V at different states of charge.

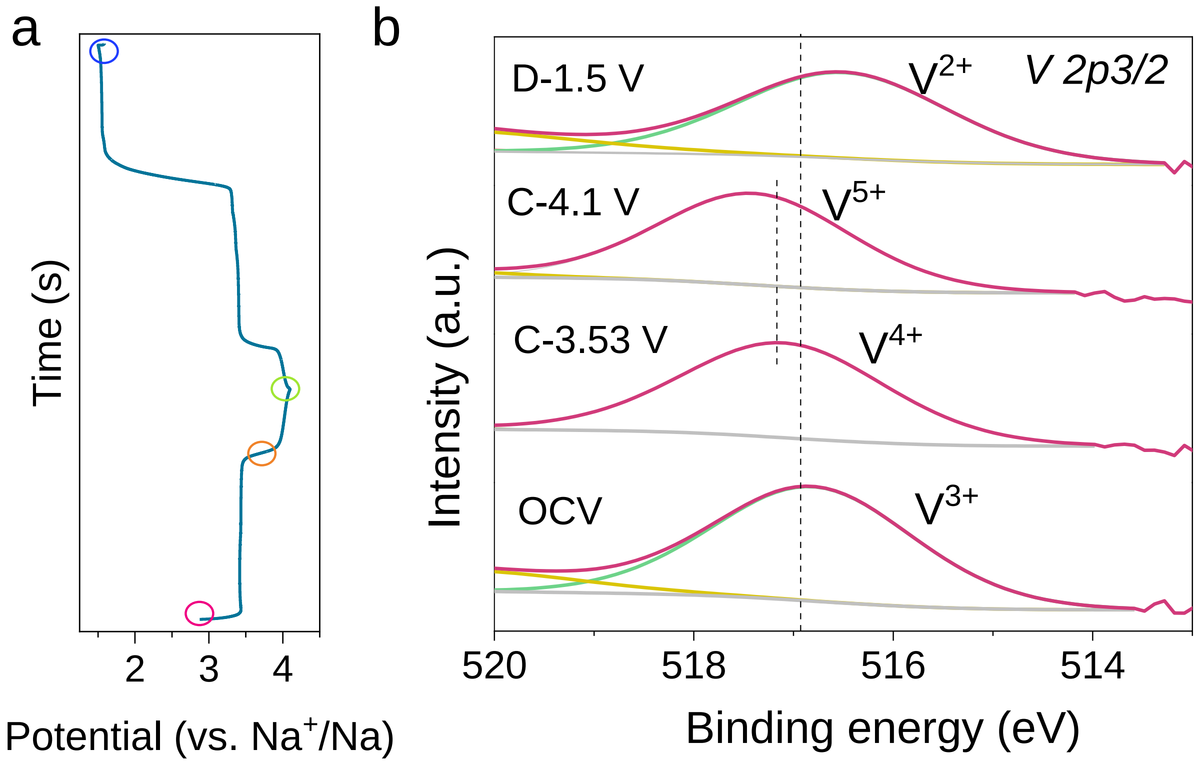

Figure S31. XPS spectra of V 2p3/2 of HE-V at different charging states.

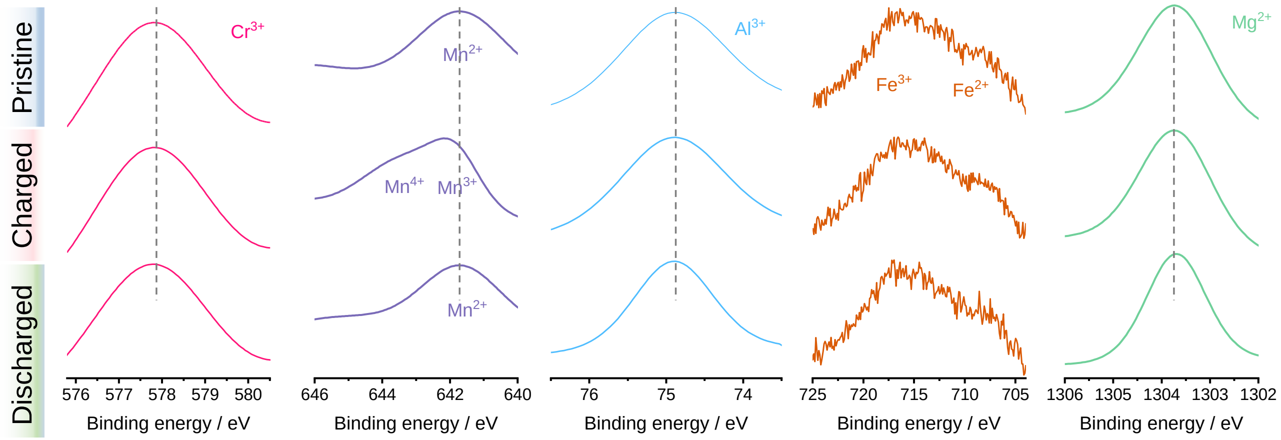

Figure S32. XPS spectra of dopants in HE-V at different states.

Note: The XPS spectra demonstrate that the oxidation states of Cr, Al, Fe, and Mg remain essentially unchanged during cycling, confirming their electrochemical inactivity throughout the charge/discharge process. A slight shift in the Mn signal suggests a potential minor oxidation from Mn^{2+} to Mn^{3+}/Mn^{4+}; however, given the low doping concentration, its contribution to capacity is negligible. These results support the conclusion that the dopants primarily serve to enhance the structural robustness and configurational entropy of the NASICON framework rather than acting as active redox centers. This finding further reinforces the entropy-engineering strategy by confirming that capacity is predominantly delivered by vanadium redox reactions.

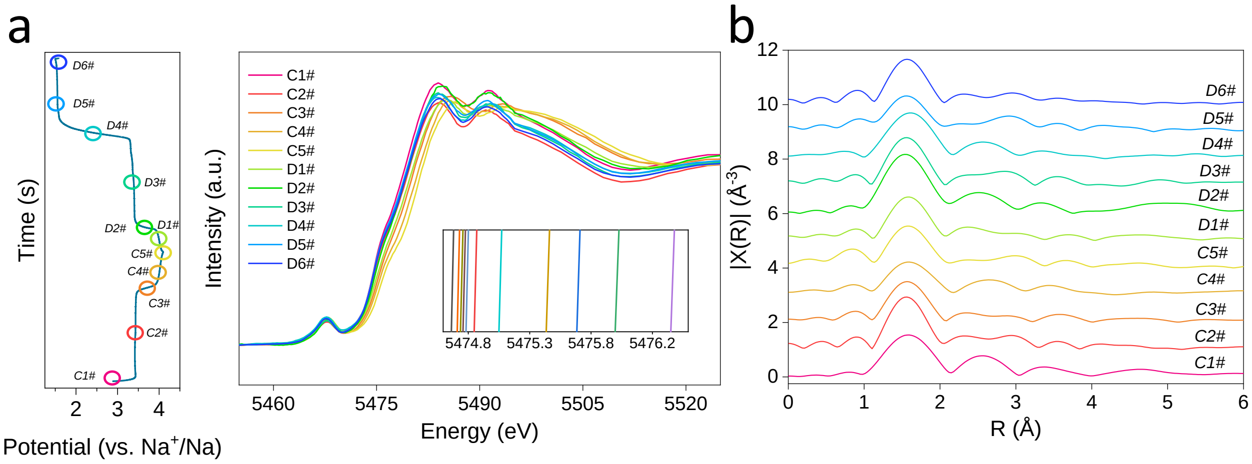

Figure S33. (a) The galvanostatic charge-discharge curve and XANES spectra at different charging states as a function of the V K-edge of the HE-V electrode and corresponding **(b)** k^2-weighted Fourier transform magnitudes of HE-V.

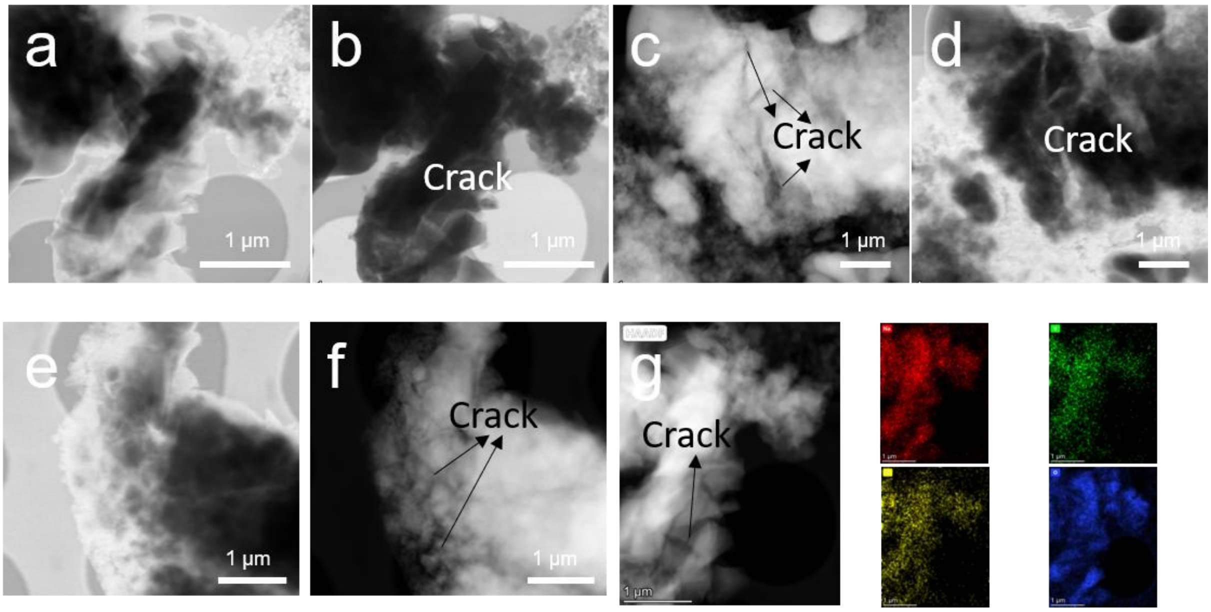

Figure S34. Postmortem analysis of the cycled NVP electrode.

*Note: After cycling, many cracks and nonuniform elemental distribution can be clearly found in the NVP particles due to the large local lattice strain and lattice defects without the help of the engineering configurational entropy strategy proposed in this work.

Supplementary references

1 B. H. Toby, *J. Appl. Crystallogr.*, 2001, **34**, 210-213.

2 S. C. Vogel, *J. Appl. Crystallogr.*, 2011, **44**, 873-877.

3 K. Momma and F. Izumi, *J. Appl. Crystallogr.*, 2011, **44**, 1272-1276.

4 W. Kohn and L. J. Sham, *Phys. Rev.*, 1965, **140**, A1133-A1138.

5 H. J. Monkhorst and J. D. Pack, *Physical Review B*, 1976, **13**, 5188-5192.

6 S. L. Dudarev, G. A. Botton, S. Y. Savrasov, C. J. Humphreys and A. P. Sutton, *Physical Review B*, 1998, **57**, 1505-1509.

7 R. Xiao, H. Li and L. Chen, *Chem. Mater.*, 2012, **24**, 4242-4251.

8 G. L. W. Hart and R. W. Forcade, *Physical Review B*, 2008, **77**, 224115.

9 S. P. Ong, W. D. Richards, A. Jain, G. Hautier, M. Kocher, S. Cholia, D. Gunter, V. L. Chevrier, K. A. Persson and G. Ceder, *Computational Materials Science*, 2013, **68**, 314-319.

10 G. Henkelman, B. P. Uberuaga and H. Jónsson, *The Journal of Chemical Physics*, 2000, **113**, 9901.

11 S. Maintz, V. L. Deringer, A. L. Tchougreeff and R. Dronskowski, *J. Comput. Chem.*, 2016, **37**, 1030-1035.

12 Z. Dai, Z. Li, R. Chen, F. Wu and L. Li, *Nat. Commun.*, 2023, **14**, 8087.